Plasma Dynamics Using Ion Doppler Spectroscopy in HIT-SI3

Charles T. Hooper

A thesis
submitted in partial fulfillment of the
requirements for the degree of

Master of Science in Aeronautics and Astronautics

University of Washington
2019

Committee:
Thomas R. Jarboe
Brian A. Nelson

Program Authorized to Offer Degree:
William E. Boeing Department of Aeronautics and Astronautics

UNIVERSITY OF WASHINGTON

Abstract

Plasma Dynamics Using Ion Doppler Spectroscopy in HIT-SI3

Charles T. Hooper

Chair of the Supervisory Committee:

Professor Thomas R. Jarboe

William E. Boeing Department of Aeronautics and Astronautics

The HIT-SI3 experiment uses three inductive helicty injectors to form and sustain a spheromak plasma by imposed-dynamo current drive (IDCD). An ion Doppler spectrometer utilizes 72 viewing chords and a μs time resolution to measure CIII impurity ions on the toroidal midplane. A Monte Carlo numerical routine is employed in conjunction with an Abel-inversion algorithm to gain insight into radial equilibrium profiles after ion spin up. Axisymmetric ion flow is calculated from the geometric axis to the inner wall along the major radius for relative density, temperature, and ion flow velocity. The profiles are then compared to magnetohydrodynamic (MHD) simulation. Time-dependent analysis show coherent sinusoidal bulk motion that is locked to the frequency of the injector perturbations indicating spheromak stability. There is evidence for ion motion in the opposite direction as the electron current in the outer injector-driven region and an ion flow reversal in the spheromak region. Relative electron density is approximately uniform from the geometric axis moving radial outwards and rapidly peaking after the magnetic axis near major radius $R = 45.5$ cm, in the same region as the maximum ion temperature.

Contents

List of Figures

List of Tables

Chapter 1

Introduction

1.1 Motivation

Energy may be one of the most, if not the most, valuable commodity in today's society. There is a growing body of evidence to suggest that a nation's per capita energy consumption is positively correlated to high standards of living, increased life expectancy, and reported quality of life among it's population.[1] If true, then it is not an exaggeration to state that it is a moral imperative to bring people out of energy poverty and increase the global power supply. This is especially so, when it is estimated that 1.2 billion people are without access to electricity and by 2040 global energy demand is estimated to rise by 30%.[2]

At this point in time, our current energy consumption is simply not environmentally or physically sustainable. Our primary energy source, fossil fuels, continue to emit greater quantities of CO_2, and have reached an all-time high in 2018.[3] Recently, in may of 2019 the atmospheric CO_2 concentration reached 415 ppm, which has not been observed on Earth for the last 2.5–3 million years.[4] A runaway greenhouse effect and distorted carbon cycle have immense societal and environmental consequences which require immediate action to mitigate the effects of compounding climate change. If new breakthroughs in technology reduced or eliminated the environmental impact of

fossil fuels, their reserves are projected to be exhausted within decades. Alternative methods of energy production are needed now more than ever.

Nuclear fusion energy has the promise to simultaneously address energy demand and climate change. A tried and true process in the universe, fusion is the nuclear process that powers main sequence stars. It's a star's immense gravitational field that creates the large temperatures and pressures necessary for fusion to be sustained, no easy task to recreate on Earth. Hydrogen nuclei undergo the proton-proton chain reaction to fuse together and form helium, releasing energy in the process. All elements that are lighter than iron produce energy when fused, with hydrogen yielding the most per nucleon. Therefore, Earth bound fusion also primarily involves merging hydrogen and its isotopes. To sustain this reaction, a hydrogen plasma temperature of about 100 million Kelvin is required, about 6 times hotter than the core of the sun but at significantly less pressure. No material could withstand this temperature for long. To prevent material contact, the plasma can be contained within within a force field created by a magnetic field. This is the basis for magnetic confinement fusion research.

A naturally occurring isotope of hydrogen, deuterium, can be easily extracted from ocean water at a low cost.[5] The ocean holds enough deuterium to power the Earth for 2 billion years using a standard steam cycle at 2007 energy consumption levels.[5] Also, consider the energy efficiency of deuterium compared to the United States leading energy source, coal. About one pickup truck bed of deuterium-laced water (HDO) can produce approximately as much usable electrical power as a volume of coal that would completely fill a $70,000$ fan football stadium.[5] In addition, fusion produces no CO_2 emissions (emitting only helium as exhaust), long-lived radioactive waste, carries no risk of nuclear meltdown, and because fusion does not use fissile materials like uranium and plutonium there is no significant nuclear weapons proliferation risk.

To benefit from all the advantages of fusion, the disadvantages must be overcome. The fundamental one being that fusion necessitates mastering the unexpectedly difficult scientific and technological problems. Great progress has been made since the theoretical anticipation of fusion in by Arthur Eddington in 1920. Although considerable effort is still needed going forward. The other disadvantage is an economical one. A fusion reactor is an inherently complex engineering project. To become a competitive energy source, novel techniques are likely needed to achieve better economies of scale. However, there is no reason to believe that these difficulties cannot be solved. In conjunction with other carbon-free technologies, nuclear fusion has the potential to become the world's principal sustainable energy source.

1.2 Plasma Confinement

An effective nuclear fusion reactor using magnetic confinement must be efficient, run continuously while sustaining the required plasma conditions, and be cost competitive in the energy market. Magnetic confinement is often attempted using fully-closed magnetic field lines. One way to generate a closed geometry is to take spatially-uniform field lines and bend them into a toroidal shape. This prevents open field lines form terminating on the inner wall of the reactor which can contaminate the plasma and damage the experiment. Unfortunately, it is well known that plasma confinement in a toroidal geometry is not in radial force balance and will expand outwards via the "tire tube" force. Toroidal fields also suffer from interchange (flute) instability. The instability is driven by magnetic pressure gradients in regions where field line curvature allows ions to escape confinement due to their larger gyroradius while confining electrons, leaving a net negative charge sheath on the confinement edge. More ions are then drawn to the edge and may escape, escalating the rate of particle loss.

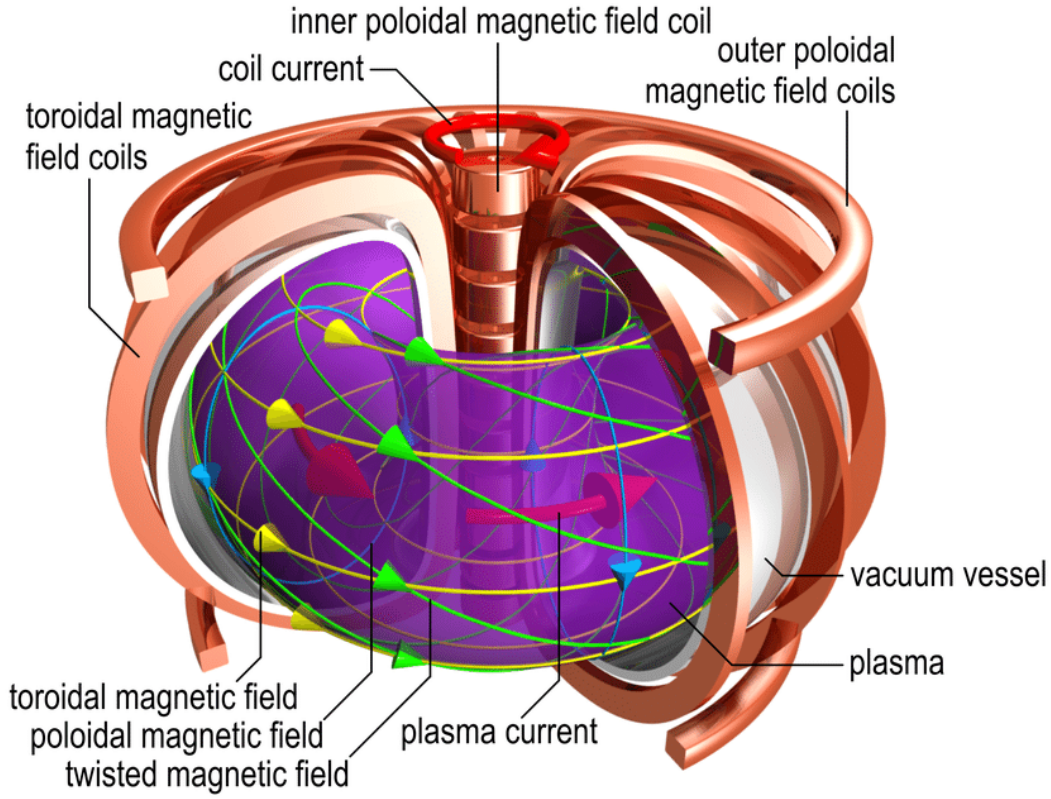

FIGURE 1.1: Basic tokamak design. The magnetic field components are, toroidal (yellow), poloidal (cyan), and the total helical field is shown in green. The three coil sets are visible, the toroidal, poloidal, and the central transformer solenoid. The latter is used to used as a primary coil to induce the toroidal plasma current (secondary). Image from C. Brandt

A method to mitigate the interchange instability is to drive a toroidal current. The plasma then generates a poloidal field that adds to the externally driven toroidal field to create a helical total field. If a vertical field component is also added, the toroidal current experiences a $\vec{j} \times \vec{B}$ force radially inward to balance the tire tube force. This is the basic design behind many magnetic confinement schemes such as the tokamak (Fig. 1.1) and the reversed-field pinch.

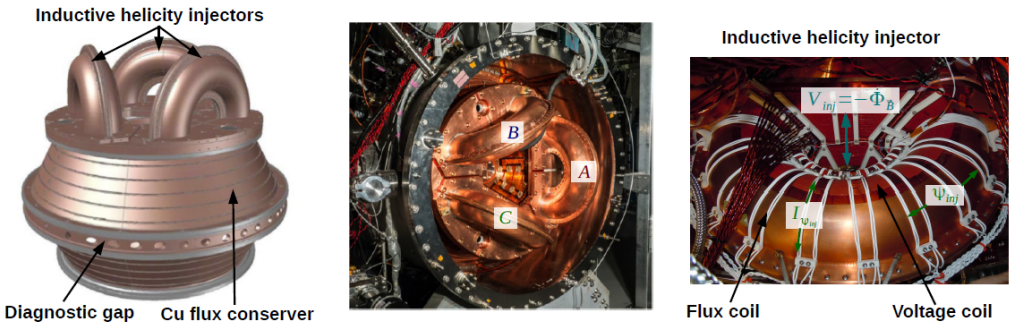

FIGURE 1.2: HIT-SI3 rendering of the flux conserver showing the three helicity injectors ("A", "B", and "C"). The flux coils (ψ_{INJ}) and voltage coils (V_{INJ}) are also depicted on the right.

1.3 HIT-SI3 and Current Drive

HIT-SI3 (Fig. 1.2) is the current stage in a development pathway to commercial nuclear fusion. It forms a plasma configuration known as a spheromak, which is conceptually appealing for fusion energy production due to their compactness, engineering simplicity, and lower projected costs as it doesn't need an expensive toroidal field coil found in tokamaks and stellerator-based designs.[6] This necessitates that the plasma itself must generate both the poloidal and toroidal fields for confinement and stability. Spheromaks are known to have sufficiently large plasma current to induce ohmic heating up to the thermonuclear operating point given high quality confinement.[5]

The predecessor of HIT-SI3, HIT-SI, is the first spheromak experiment designed to both form and sustain a spheromak using only induction.[7] HIT-SI3 uses three purely inductive helicty injectors each separated by a constant temporal phase $\Delta\phi$. The solenoid free startup uses what is known as steady inductive helicity injection (SIHI) to inject magnetic flux into a simply connected bow tie shaped flux conserver. The helicty injectors are driven at a fixed frequency. For data presented here, the injector frequency is $f_{INJ} = 15.6$ kHz. On timescales of interest in the spheromak, magnetic helicty is approximately constant such that a plasma configuration will relax itself into an

equilibrium that minimizes its magnetic energy to reach an eignestate of the flux conserver while conserving helicity.[8] This drives a toroidal current in such a way as to ohmically heat the plasma. The theoretical basis for steady state sustainment has been shown to be sufficiently explained by the theory of "Imposed-Dynomo Current Drive"[8] (IDCD). A stable equilibrium has been shown to be efficiently sustained with imposed fluctuations and the current profile can, in principle, be controlled. Both are significant steps for controlled fusion partly because a lack of efficient steady-state current drive and profile control causes disruptions in tokamaks.[9] Questions still remain on the quality of confinement and weather the applied perturbations have a meaningful effect on the structure and dynamics of the spheromak.

Chapter 2

Ion Doppler Spectroscopy

2.1 Theory of Ion Doppler Spectroscopy

Due to the extreme conditions often found inside laboratory plasmas, physical probes to analyze plasma behavior are not always ideal as they can introduce impurities and disrupt particle transport. For these reasons, passive diagnostic techniques have become an important foundation in experimental plasma physics. While there are many different types of observed radiation, including electron cyclotron emission (ECE) and bremsstrahlung, ion Doppler spectroscopy utilizes the emission lines from bound electron transitions. Impurities in a plasma may possess bound electrons that are collisionally excited to an orbital energy level corresponding to energy E_i. The electron will then spontaneously decay to a lower energy level E_j and emit a photon that has energy equal to the difference of the two states, $h\nu_{ij} = E_i - E_j$, where h is Plank's constant and ν is the frequency.

The rate of spontaneous emission is found from the Einstein coefficient A_{ij}. A_{ij} is an inherent property of the atom of interest and therefore holds for any type of radiation. An order magnitude estimate[10] of the average decay time is found to be $\approx 10Z^{-4}$ ns where Z is the ion charge number. After considering the operation time and densities for HIT-SI3 (about 2 ms and 10^{19} m^{-3}) the plasma may be considered to be in coronal equilibrium. All upward transitions are assumed to be collisional and all downward transitions are

radiative. Significant radiation is assumed to escape, not to be reabsorbed. In other words, the plasma is considered optically thin and the downward transitions are independent of density.

Energy fluctuations in the surrounding space of a transitioning bound electron create a natural line broadening in observed transitions due to the quantum mechanical uncertainty principle. For frequencies in the visible spectrum and for pressures in HIT-SI3 this broadening is negligible. The emission line may be assumed to be monoenergetic. However, thermal effects in the plasma give rise to a broadening of the emission line. This thermal broadening is described by the Doppler effect which is the change in frequency between the laboratory frame and the frame of the wave source. When waves are moving toward the observer the wave fronts tend to compress or "pile up". Conversely, if the waves are traveling away from the observer the distance between the wave fronts increases and the waves "spread out". Therefore, an ion traveling at velocity v_i and emitting a photon at wavelength λ_0 in the source frame will experience a wavelength shift of $\Delta\lambda = \lambda - \lambda_0$ to an observer in the lab frame. To a stationary observer in the lab frame this shift is given by the Doppler formula,

$$v_i = c\frac{\Delta\lambda}{\lambda_0} \qquad \left[\frac{m}{s}\right] \tag{2.1}$$

where c is the speed of light. The mean velocity shift of a thermal population of ions in a plasma is called the ion or flow velocity.

HIT-SI3 features a collisional plasma and is assumed to equailibrate locally into a Mawellian distribution. In one dimension the particle distribution is

$$f(v_i) = \sqrt{\frac{m_i}{2\pi k_B T}} exp[\frac{-m_i v_i^2}{2k_B T}] \tag{2.2}$$

where k_B is the Boltzmann constant, m_i is the ion mass, and T is the ion temperature. It is possible to substitute for v_i with Eq. 2.1 to obtain the broadening profile in terms of observed wavelength in the laboratory frame.

$$f(\lambda) = \sqrt{\frac{m_i}{2\pi k_B T}} exp[\frac{-m_i c^2(\lambda - \lambda_0)^2}{2k_B T \lambda_0^2}] \tag{2.3}$$

Now one can solve for the temperature in terms of the emitted source frame wavelength and the standard deviation σ of the Gaussian distribution.

$$T = \frac{\sigma^2 c^2 m_i}{\lambda_0^2 k_B} \qquad [eV] \tag{2.4}$$

Different ion species in a plasma may in general have different temperatures. If it is assumed that the impurity species (2) is considerably heavier than the majority species (1) and μ is the mass (amu) then the impurity ion thermalization rate occurs at collision frequency given by Eq. 2.5.[11]

$$\nu \sim 10^{-12} \frac{\sqrt{\mu_1}}{\mu_2} \frac{n_1 Z_1^2 Z_2^2}{(T_1/e)^{3/2}} \qquad [s^{-1}]. \tag{2.5}$$

Using $T_i = 15$ eV and $n_e \sim 10^{-19}$ m^{-3} (typical values recorded in HIT-SI3[12]) temperature equilibration occurs on the order $\sim 10^{-5}$ s for CIII impurities in a deutirium-dominant plasma. Therefore, it is safe to assume that the impurity temperature measurements after 1 ms are representative of the dominant ion temperature.

It is also important to consider different effects that would change the shape of the emission profile since Eq. 2.4 holds only as long as the observed emission profile is in fact Maxwellian. If the plasma pressure is too high, micro-electric fields near an emitting atom will shift the transition energy required. This is known as Stark broadening and has a Lorenzian broadening profile. The observed signal would then be a Voigt profile and deconvolution

techniques would need to be employed to resolve the temperature broadening. It is reasonable to assume, $||\vec{E}||$ and $||\vec{B}||$ are low enough such that Stark, Zeeman, and other higher order effects are negligible in the detected emission profile. For the case of the CIII the spectral profile is affected when the shifts become relevant at two and three orders of magnitude higher than observed density[13] and field,[14] respectively.

2.2 IDS Experimental Apparatus

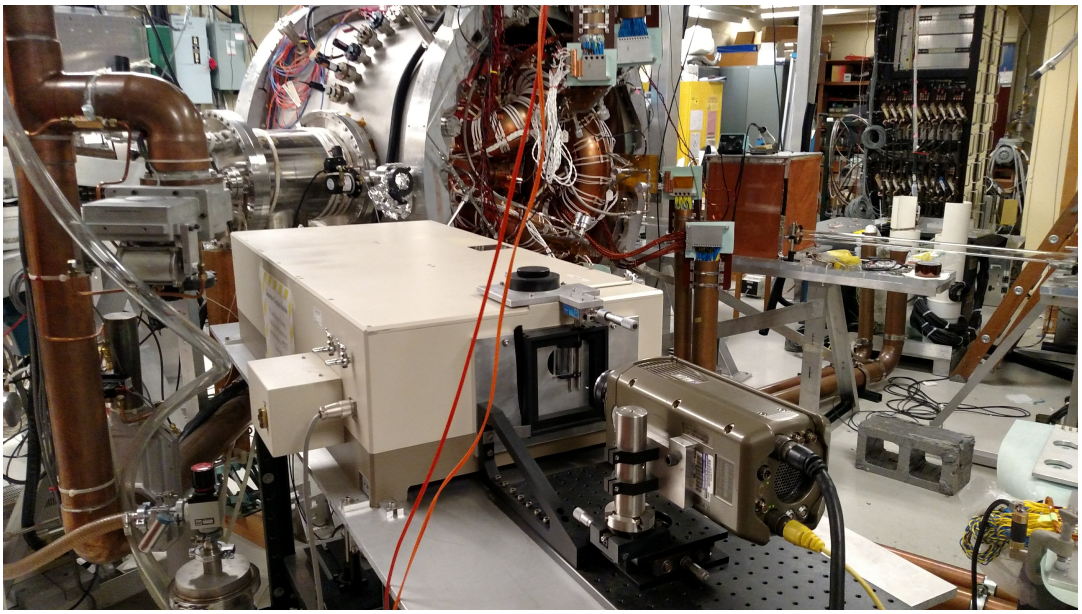

FIGURE 2.1: The IDS diagnostic in operating position.

2.2.1 Spectrometer Overview

The diagnostic setup (Fig. 2.1) used for IDS is a 1 m focal length, MC-100 (Czerny-Turner configuration) spectrometer on loan from Professor Nagata at the University of Hyogo in Japan. Specifications are given in Table 2.1. The beam path is shown in Fig. 2.2. The entrance slit width is adjustable and

there is a collimating lens over the exit slit as the vertical and horizontal focal planes do not focus at the same axial location. The light emanating from the exit slit is detected by a Phantom v710 fast camera from Vision Research International. A motor is attached to the side of the spectrometer for automatic adjustment of the diffraction grating, and is used for calibration. The spectrometer is mounted onto a large cart with stabilizing docking pegs to minimize mechanical vibrations. The spectrometer dial gives the displayed wavelength

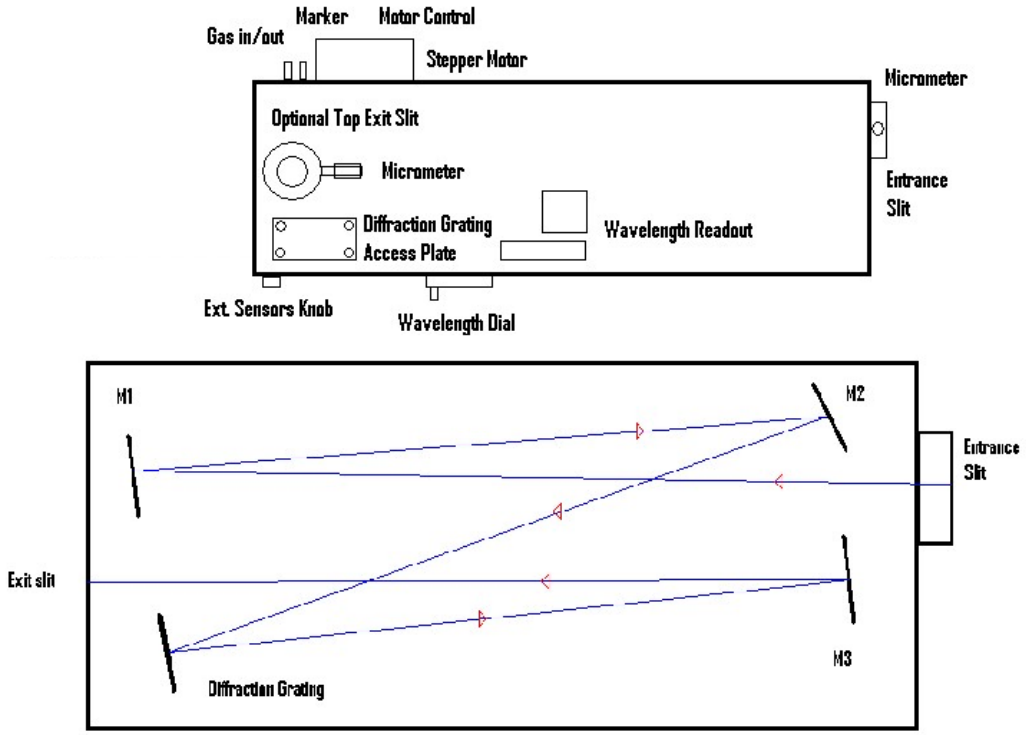

FIGURE 2.2: Two different top-down views of the spectrometer. The upper most diagram shows different features and their location. The bottom view shows the signal beam path, mirrors (M), and diffraction grating

2.2.2 Fibers and Entry Ports

There are two fused silica fiber optic cables that are mounted to the entrance slit. Each cable or fiber bundle contains 36 individual fibers (channels) each 3

Specification:	**Value:**
Wavelength Range	250 - 700 [nm]
Collimator Focal Length	1,000 [mm]
Focal Ratio	f/8.5
Diffraction Grating Groove Density	1,800 [grooves/nm]
Diffraction grating Blazed Wavelength	250 [nm]
Diffraction Grating Dimensions	102×102 [mm]
Wavelength Selection	Sine Bar Method
Wavelength Display	Counter Device
Smallest Wavelength Increment	0.1 [nm]
Slit Width	80 [μ m]
Smallest Slit Width Increment	10 [μm]
Slit Height	20 [mm]
Wavelength Precision	$\pm$0.05 [nm]
Wavelength Duplicability	$\pm$0.05 [nm]
Resolution (Half Height)	0.009 [nm]
Wavelength Purity	0.49 [nm/mm]
Optical Axis Height	180 [mm]
High-Pass Cutoff Light Filter	280 - 900 [nm]
Diffraction Grating Replaceable	Feasible
Exterior Dimensions	$1090 \times 530 \times 280$ [mm], 80 [kg]

TABLE 2.1: Spectrometer Physical Parameters

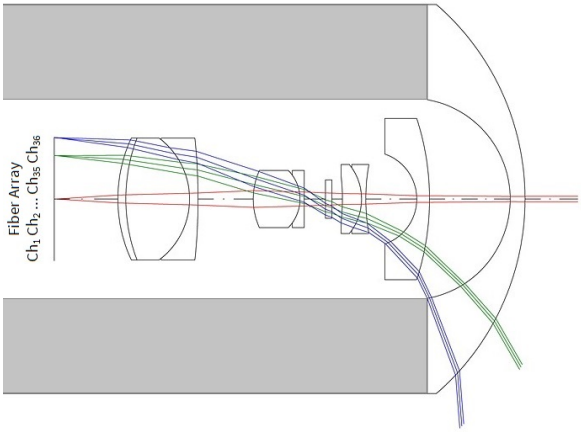

FIGURE 2.3: A cross section of the upper fiber bundle with lens and approximate ray trace diagram and aluminum housing (gray). Each channel in the linear array receives a source throughput that is dependent on the viewing angle from central axis.

m long and arranged linearly. The channels are labeled from $1-72$. Channel 5 is dead and doesn't receive light. Aluminum fiber holders are machined to fit into the re-entrant ports where plasma light is imaged onto each linear fiber array in each cable by a wide-angle "Micro Video Lens" from Edmund Optics. It is important to keep in mind how the light is mapped through the lens to the fibers. Fig. 2.3 shows a ray trace diagram where the rays along the line of sight (chord), do not correspond to the nearest channel but to the channel opposite the central axis of the lens. Each fiber receives a cone shaped volume of light that is 5.1 cm at the vacuum vessel wall and each of these light-cones are separated by approximately 2.95° at a distance of $\sim$ 110 cm, the approximate diameter of HIT-SI3. The ± 8 midplane half-nipple or "Mohawk" ports are on the toroidal midplane ($\pm 85.34°$ from the horizontal plane in Fig. 2.4) allowing data to be collected on chords that fan out from the port location. The center line of each fiber array is oriented $\pm 39.17°$ relative to the center of curvature of the outer vessel. Data collected span from the geometric axis to the wall.

The geometric orientation of each fiber's chord is represented by an impact parameter, or distance of closest approach to the geometric axis. The impact parameters are arbitrarily chosen to be positive above the horizontal plane going through the geometric axes and negative below as viewed in Fig. 2.4.

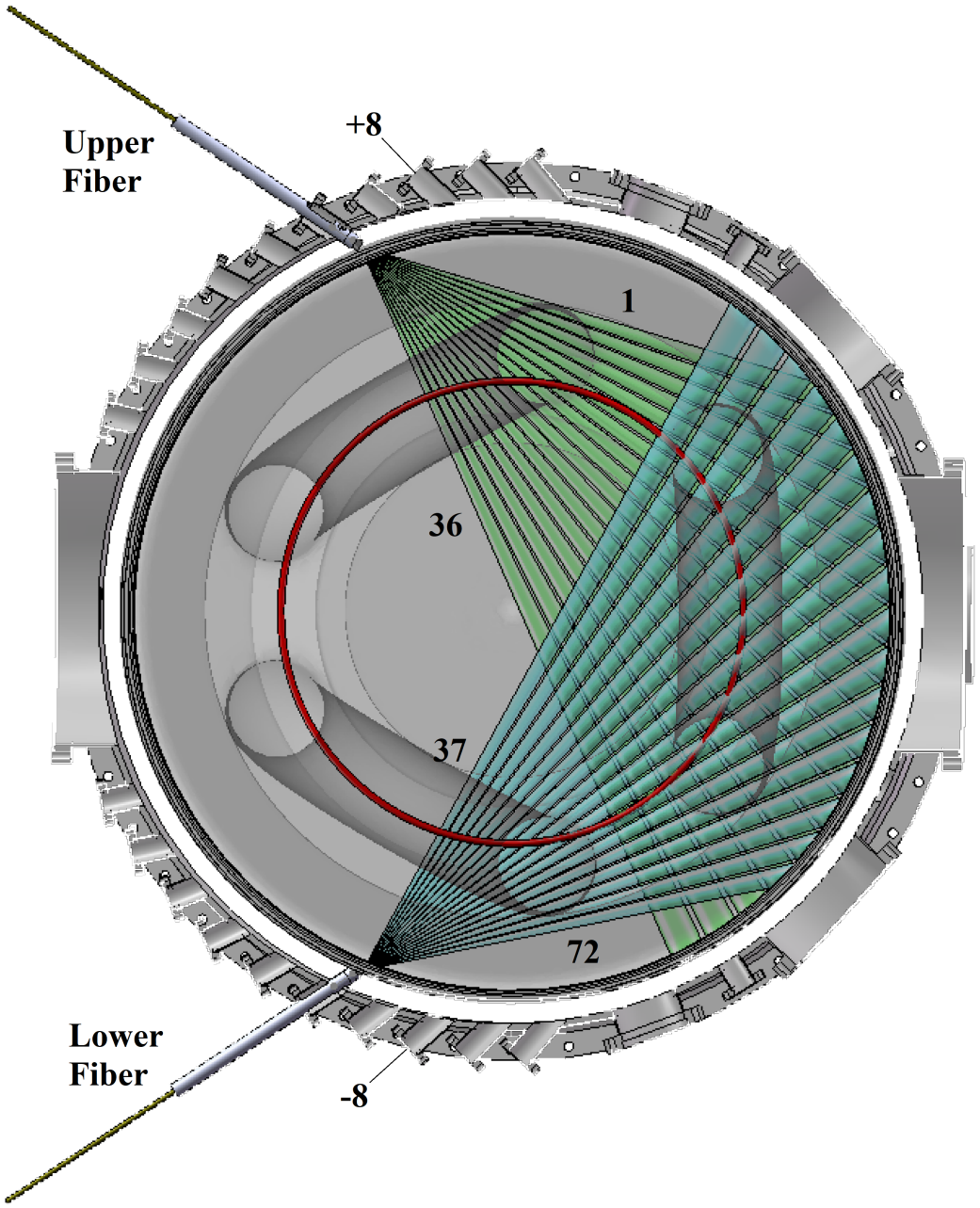

FIGURE 2.4: A lab frame, injector side, view of the toroidal midplane cross section of HIT-SI3 depicting the magnetic axis (red) and the semi-transparent rendering of the injectors. The upper and lower fiber bundles and their viewing chords are shown in the ± 6 Mohawk re-entrant ports. The location of the ± 8 mohawk ports ports being used in this study are labeled. On the upper fiber bundle, channel 1 sees the top chord and channel 36 views the lowest chord. On the lower fiber bundle, channel 37 sees the upper most chord and 72 the lowest.

Chapter 3

Data Acquisition

3.1 Calibration

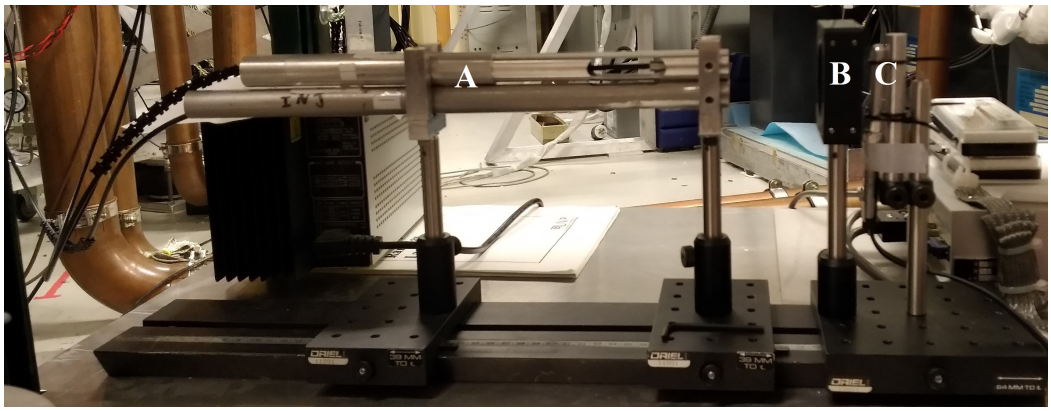

FIGURE 3.1: The calibration stand set up directly underneath the spectrometer. A is the two aluminum fiber holders housing the two fiber arrays. B is the ground glass diffuser and C is the UVP mercury lamp.

IDS calibration is necessary to obtain the measure the amount of broadening due to the instrument (instrument temperature), the wavelength separation of camera pixels (dispersion), and the relative intensity of each fiber. These variables need to be found empirically with a spectral line near the wavelength of the plasma lines of interest. This has been done using the 435.84 nm spectral line from a UVP mercury pen lamp. The signal is recorded with the camera properties seen in Table 3.1.

Specification:	Value:
Resolution	320 × 211 [pixles]
PPS	120 [Hz]
Exposure	8300 [μs]
Motor Speed	0.1 [nm/s]

TABLE 3.1: Camera Calibration

3.1.1 Instrument Temperature

The fiber bundles are stacked and secured on a stand with set screws directly in front of a ground glass diffuser. Both fiber bundles are oriented to be aligned completely vertical without their wide-angle lens. On the opposite side of the diffuser, a stand holding the pen lamp is in place. The spectrometer is dialed to capture the 435.84 nm mercury line. The signal is captured by the fast camera with the linear fiber arrays now aligned horizontally in the middle of the CCD and (Fig. 3.2) and a video is recorded. Afterwards, the movie file is converted into a MATLAB file. The MATLAB script converts each frame of the movie to an $n \times m$ intensity matrix with arbitrary intensity units. Each matrix has an associated time stamp. This matrix then undergoes biorthogonal decomposition (BD) before being fit with a normal distributions as shown in Fig. 3.2. This filtering method reduces the noise surrounding each Guassian and is explained by Hossack.[15]

The light from each fiber is individually fit to a 2D normal distribution of the form Eq. 3.1 for each time frame of the movie and averaged.

$$f(x,y) = \frac{V}{2\pi\sigma_x\sigma_y} exp\left(-\left(\frac{1}{2}\frac{(x-x_0)^2}{\sigma_x^2} + \frac{(y-y_0)^2}{\sigma_y^2}\right)\right) + f_0 \tag{3.1}$$

Here, V is the "volume" of the normal distribution, x is the spatial direction, y

is the wavelength direction, x_0 and y_0 are the centroid locations, and σ is the standard deviation. Note that using a volume parameter instead of an amplitude parameter allows the fitting parameters to be independent. The centriods identify the fiber spatial positions on the CCD relative to one another taking into account changes due to vibrations from moving the spectrometer and relative offsets in the wavelength direction due to curvature from the optics. σ_y is used to estimate the instrument temperature T_{int} from Eq. 2.4 to yield $T_{int} \in [12 - 16]$ eV.

3.1.2 Dispersion

The spectrometer's grating is moved at a precise rate (Fig. 3.1) with a stepper motor. Otherwise, the physical set up is identical to Section 3.1.1. The motor is used to record the centroids moving up the CCD in wavelength space, each time frame is fit with a normal distribution for each fiber channel. The centroids of each distribution are tracked in MATLAB along their path as shown in Fig. 3.3. The centroid distance through wavelength space vs. time is fit linearly with a least squares regression. The slope of which determines the dispersion. The value is consistently $\approx 1.179 \times 10^{-11}$ nm/pixel. This conversion factor makes it possible to convert all the the raw CCD data from pixels to wavelength.

3.1.3 Intensity

Each fiber bundle with its wide-angle lens is secured one at a time to a rotational stand facing the UVP pen lamp. The diffuser ensures even illumination of each individual fiber. The alignment of the fiber array is now completely horizontal. Once the camera is recording, the stand is slowly rotated through 180°. This allows each individual fiber to reach a point in which it receives maximum throughput from the light source. The intensity at each centriod

calculated from Eq. 3.1 and are plotted vs time (Fig. 3.4). The peak of which designates a time frame of maximum intensity for that fiber. For this time frame, a normal distribution is fit. This process is repeated for all fibers. The relative intensity $I_{rel} = A/\overline{A}$ is defined as the area under the distribution divided by the mean area for all fibers. The area used is in the wavelength direction only because of overlap by the neighboring fibers in the spatial direction. The amplitude and area are calculated respectively as follows.

$$A = \frac{V}{2\pi\sigma_x\sigma_y} \tag{3.2}$$

$$a = \sqrt{2\pi}\sigma_y A \tag{3.3}$$

This calibration also presents an opportunity to to check the center line of each fiber array. The angle ticks on the rotational stand are used to ensure that the fiber bundle is co-linear with the light source. Ideally, the exact center of the fiber array should be illuminated. If this is not the case, the actual center of illumination is reflected in the impact parameter calculations.

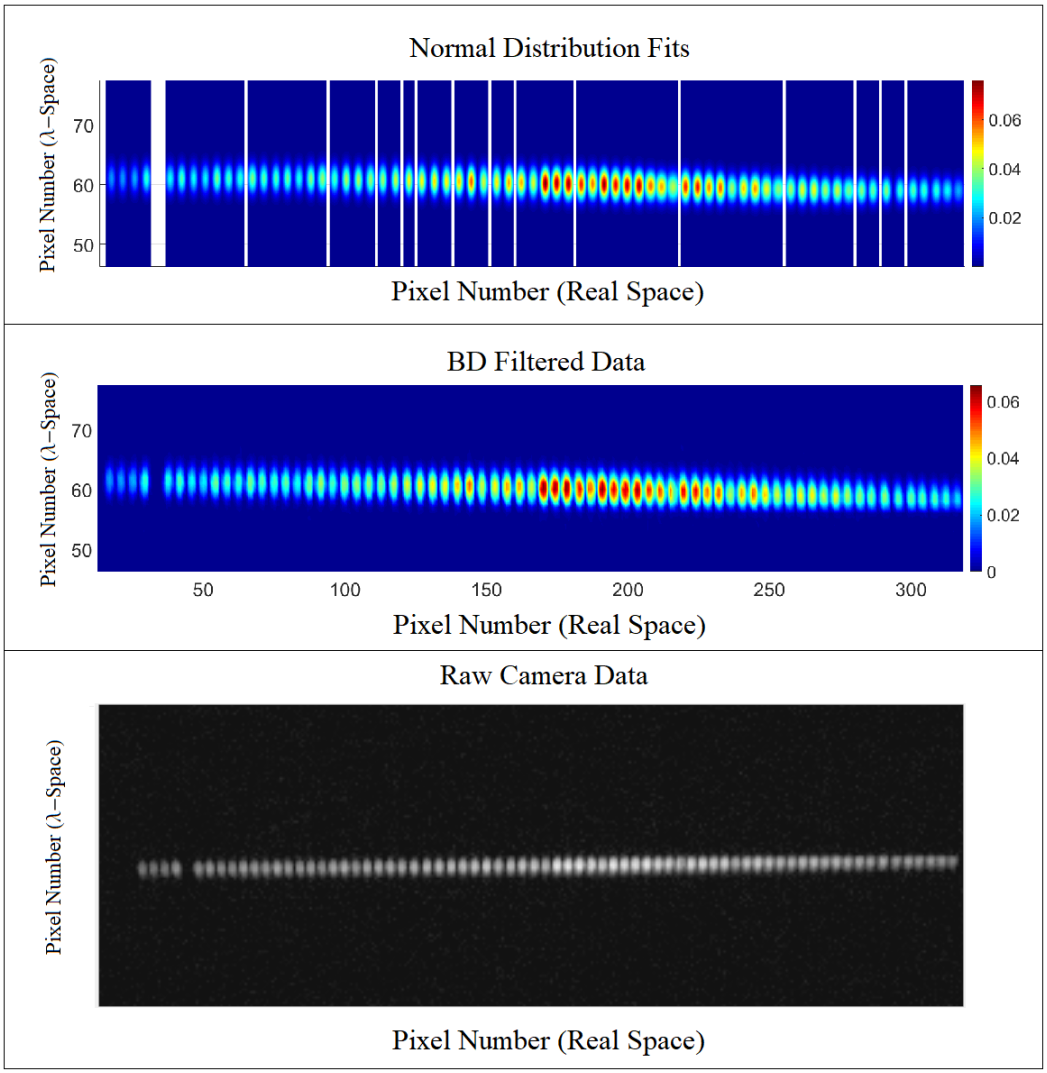

FIGURE 3.2: The raw camera data (bottom, axes not to scale) is shown along side the BD filtered MATLAB data (center) and the normal distribution fits (top). The fiber channels are ordered from left (1) to right (72). Channel 5 is dead.

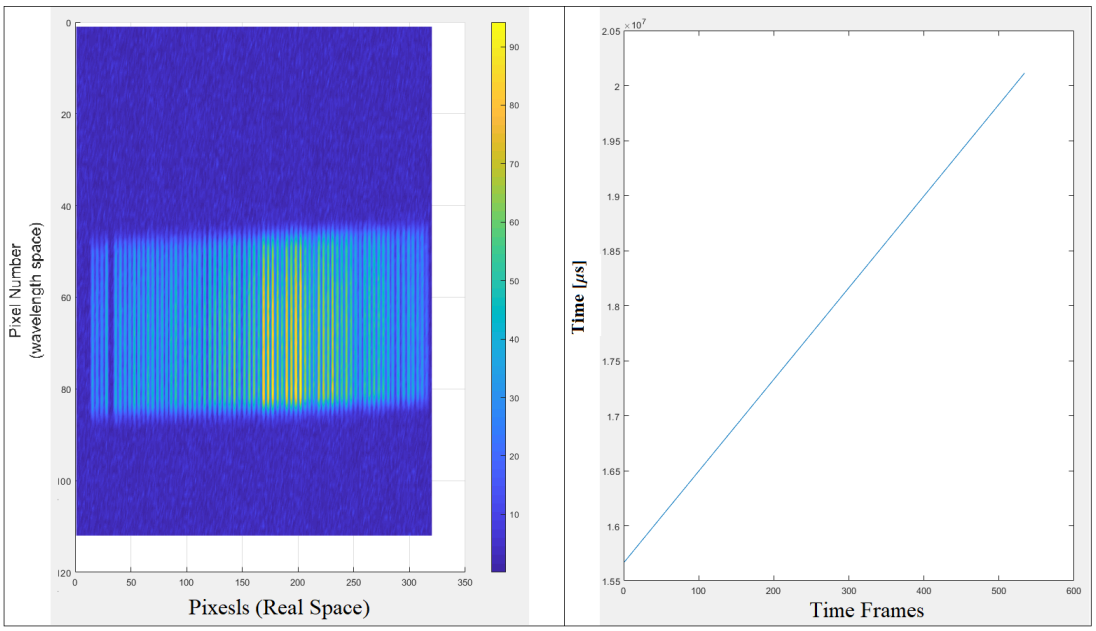

FIGURE 3.3: Raw data is shown with each time frame superimposed. The camera time assigned to each time frame is shown on the right.

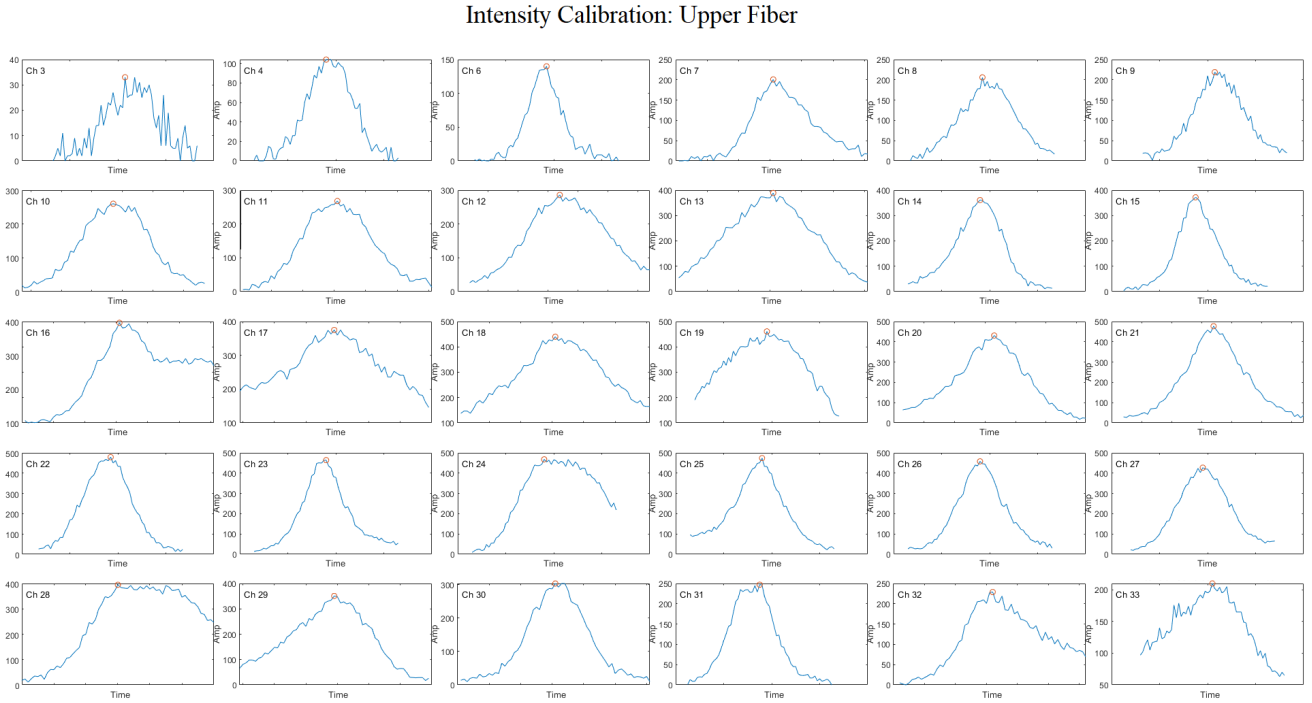

FIGURE 3.4: The intensity is plotted for each fiber centroid vs time. The upper fiber bundle chords $3, 4, 6 - 33$ are shown here. The red point on each plot indicates the time frame used for calibration. Notice that the edge channels shown have lower signal to noise ratios.

3.2 Levenberg-Marquardt Method

The model function $f(x, y, \mathbf{a})$ (Eq. 3.1) is fit to the data using the Levenberg-Marquardt Method (LMM). Here **a** encapsulates the fitting parameters, f_0, x_0, y_0, σ_x, σ_y, and V. LMM is a damped least-squares method that combines two minimization methods: the Gauss-Newton method and the gradient descent method. In the Gauss-Newton method, the sum of the squared errors is reduced by assuming the least squares function is locally quadratic, and finding the minimum of the quadratic. In the gradient descent method, the sum of the squared errors is reduced by updating the fitting parameters in the direction of the greatest reduction of the least squares objective. LMM has been used previously[12] to solve non-linear least squares problems for IDS. The method finds the minimum of a function $\boldsymbol{F}$ that is a sum of squares of nonlinear functions. The set of unweighted equations in Eq. 3.4 is following the implementation given by Gavin.[16]

$$\left(\mathbf{J}^{\mathbf{T}}\mathbf{J} + \lambda\mathbf{I}\right)\boldsymbol{\delta} = \mathbf{J}^{\mathbf{T}}\left(\mathbf{F} - \mathbf{f}\right) \tag{3.4}$$

J is the Jacobian. The (non-negative) damping factor is adjusted at each iteration and is initially stepped by $\lambda = 0.001$. λ scales by a factor of ten in the direction of the change in χ^2. Decreasing λ will make the algorithm closer to the Gauss-Newton method, while increasing λ gives a step size $\boldsymbol{\delta}$ closer to the gradient-descent direction. The vector $\boldsymbol{\delta}$ is updated with each iteration until the sum of the squares of the errors between the data points and the function is minimized. When this condition is satisfied, the parameter vector **a** is considered to be the solution that comprises the final fit $\boldsymbol{f'}$.

LMM allows the calculation of the overall model error as well as the individual parameter errors. The sensitivity of which is scaled by the overall root mean square (RMS) error of the fit, producing standard parameter errors. It is then straightforward error propagation to directly obtain the error

of plasma parameters of interest. The LMM error makes use of the following model,

$$\sigma_p^2 = \text{diag}\left(\text{covariance}(f')\right) = \text{diag}\left(\sigma_{RMS} H^{-1}\right) = \text{diag}\left(\sigma_{RMS}\left[J^T J\right]^{-1}\right) \tag{3.5}$$

where $\boldsymbol{H}$ is the Hessian matrix and is approximated by $\left[J^T J\right]$ assuming small higher order residuals. All the fitting algorithms discussed in this section are implemented in the *lm* MATLAB package.

3.3 Plasma Signal

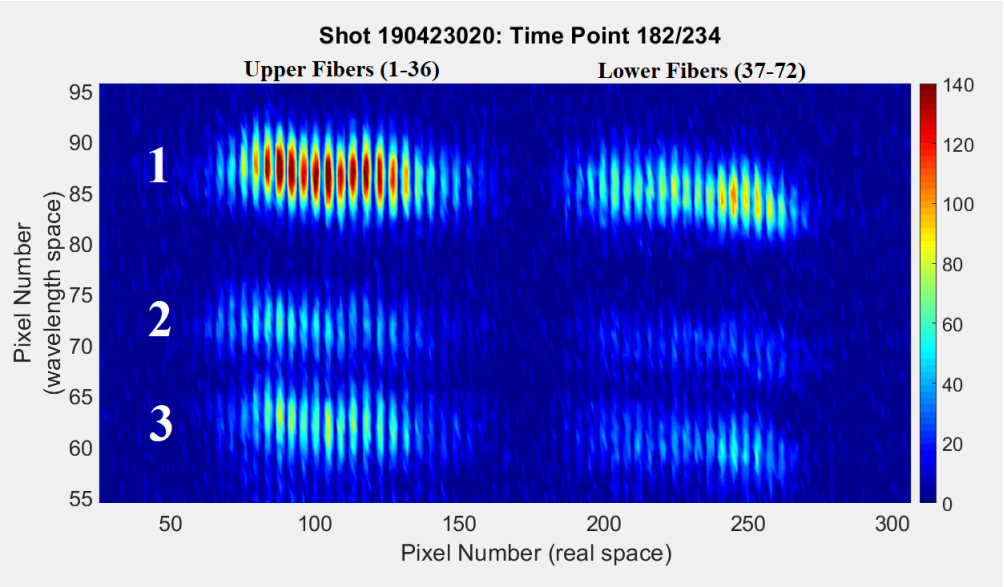

FIGURE 3.5: Highest amplitude time frame of raw shot data from the CCD display. The three strongest lines shown are CIII = 464.74 nm (line 1), OII = 464.91 nm (line 2), and the CIII = 465.025 nm (line 3). A fourth line (CIII = 465.147 nm) is present just below the CCD.

$$1s^2 2s3P\left({}^3P\right) \Longrightarrow 1s^2 2s3s\left({}^3S\right) \qquad 464.74 \text{ nm CIII (triplet)} \tag{3.6}$$

$$2s^2 2p^2 \left({}^3P\right) 3p \left({}^4D\right) \Longrightarrow 2s^2 2p^2 \left({}^3P\right) 3s \left({}^4P\right) \qquad 464.91 \text{ nm OII (quartet)} \tag{3.7}$$

In HIT-SI3 measured radiation is dominated by two line spectra given defined by equations 3.6 and 3.7. The two other higher wavelength lines form the CIII triplet can be seen on the CCD. In past experiments[12,15] that operated at lower values of f_{INJ} the OII line had large enough amplitude for confident resolution. As can be seen in the highest intensity time frame in Fig. 3.6, there is significant signal overlap present between all lines except CIII $=$ 464.74 nm. Hence, the individual signals for other lines cannot be resolved for the plasma shots analyzed here.

Before data collection the camera is set to continuously record data and the spectrometer is tuned to 465 nm. When a plasma shot starts, the server sends out a trigger signal to mark the exact start time of SIHI. The camera then records a set amount of post trigger time frames under the settings given in Table 3.2. A shot lasts $\approx$ 2.2 ms with satisfactory line emission intensity for the last $\approx$ 1.2 ms.

After data is collected, a fitting window is centered on each spectral line under investigation. No BD filtering is used as opposed to past experiments.[12,15] The channels on each time frame are individually fit by the same procedure as described in the calibration section 3.1.1. The temperature measured is a convolution of both T_{inst} and the ion temperature T_i Gaussian profiles and the measured width is then related by Eq. 3.8

$$\sigma^2_{total} = \sigma^2_{T_i} + \sigma^2_{T_{inst}}. \tag{3.8}$$

From Eq. 2.4 $T \propto \sigma^2$ and we obtain the deconvolution Eq. 3.9,

$$T_i = T_{total} - T_{inst} \tag{3.9}$$

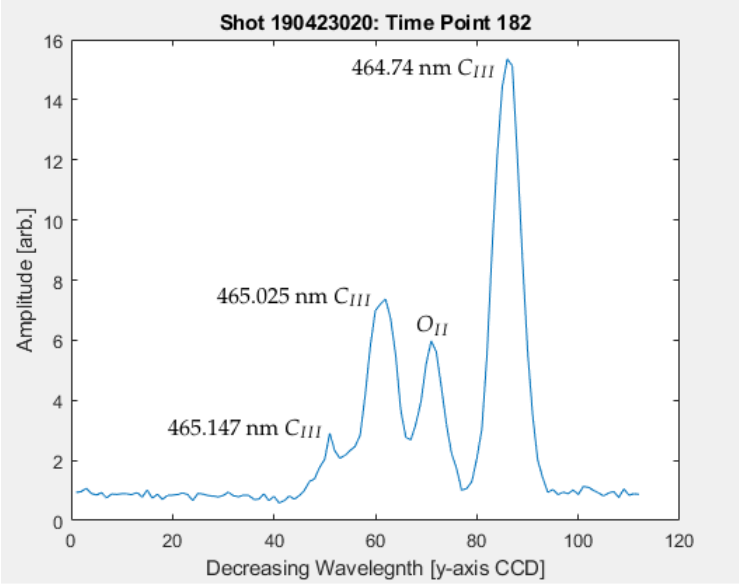

FIGURE 3.6: A single time frame of raw data from the CCD display. Relative signal amplitude is shown for CIII lines and OII.

where taking the difference would produce another Gaussian. Hence, the ion temperature T_i can be analytically deconvolved by simply subtracting off T_{inst}.

Specification:	**Value:**
Resolution	320 × 211 [pixels]
PPS	93.66 [kHz]
Exposure	10 [μs]
Post Trigger Frames	200

TABLE 3.2: Camera settings during data collection

3.4 Fitting Plasma Data

Plasma temperature is positively correlated with toroidal current I_{TOR}. Significant toroidal current, $I_{TOR} > 50$ kA or current gain above 2.2, is required to ensure a strong intensity signal that allows the majority of individual fits

to converge. Even with these conditions met, without the filtering effects provided by BD, there are blanks in the fitted data. An example is shown in Fig. 3.7 channel 8. Blank data are due to a few reasons and are more likely to affect the fibers on the innermost and outermost locations of each fiber bundle (1–8, 30–36, 37–42, 65–72). The primary reason is the LMM itself fails to converge to a minimum. Either from spatial overlap of the distributions (Fig. 3.7 channel 34) or from signal background noise (Fig. 3.7 channel 10). A causal factor is that the chords aligned to the outer edge of the plasma have a weaker signal. The chord length is shorter and hence receives a smaller signal since there is less light integrated over the chord length. Also, the wide-angle lens reduces intensity on these channels and is evident from the small amplitutes for channel 3 and 33 in Fig. 3.4. Another possibility for blank data points is that a solution converged but had too large an error and was intentionally excluded from the data set. A fit with percent error in σ_y or y exceeding 1.5 pixels are discarded.

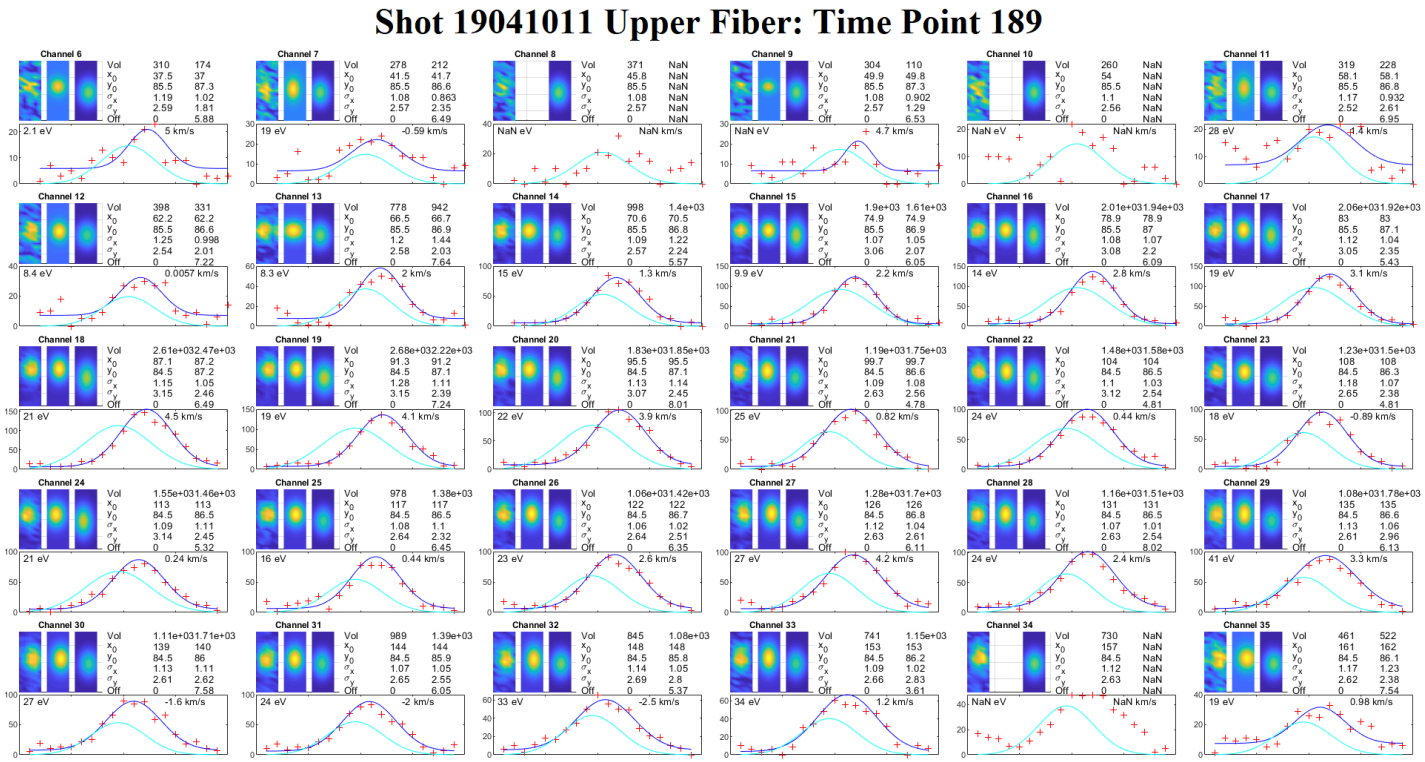

FIGURE 3.7: A single time point of a deuterium plasma shot C_{III} line with $I_{TOR} = 75.2$ kA and a toroidal current gain 2.70 for channels 6–29. For each fiber shown there are three overhead Gaussian subplots under the channel name. These plots show initial guess parameters for the LMM obtained from calibration (right), the fit for the data (middle), and the raw data (left). The initial guess parameters are shown in the left column and the fit parameters in the right column. There is also a 2D cross sections of the fit (dark blue) and the initial guess (light blue) in the wavelength direction for each channel. The red crosses are the raw data points. Temperature and velocity are shown as well.

Chapter 4

Results

4.1 Relative Density

Chord length normalized intensity measurements were used to make an estimation of relative density. In an optically thin, low density plasma in coronal equilibrium, one can calculate the power emitted[17] in a transition from level i to j $(E_i > Ej)$ by Eq. 4.1,

$$P_{ij} = n_e n_{ion} R_{ji} B_{ij} E_{ij} \tag{4.1}$$

where n_{ion} and n_e are the ion and electron number densities respectively, R_{ji} is the rate coefficient for collisional excitation induced by electrons from ground state j to excited state i, B_{ij} is the radiative branching ratio for decay to state j, and $E_{ij} = E_i - E_j$ is the energy released in the bound electron energy level transition. As part of the coronal approximation all upward transitions are assumed to be from electron induced collisions from j to i only. The radiative intensity of a transition then scales as,

$$I_{ij} \propto n_e n_{ion} R_{ji}$$

because the power detected is proportional to the photon flux per time interval of the transition E_{ij} and B_{ij} are constant. R_{ji} is expected to change

little throughout the plasma over an injection cycle as pressure and temperature gradients are not exceptionally large. Furthermore, $n_{ion} \propto n_e$ since it is assumed the ionization rate is proportional to n_e. Therefore, the electron density roughly scales as

$$n_e \sim \sqrt{I_{ij}},$$

where I_{ij} is the volumetric intensity and has units of counts/m^3. The relative density distribution as a function of time can be seen in Fig. 4.1. The relative density and the temperature are both positively correlated with the toroidal current amplitude (Fig. 4.1 and Fig. 4.2) as heating and compression appears synchronized with the total injector current perturbations. Areas with large error (indicated by the red regions) are excluded from analysis going forward

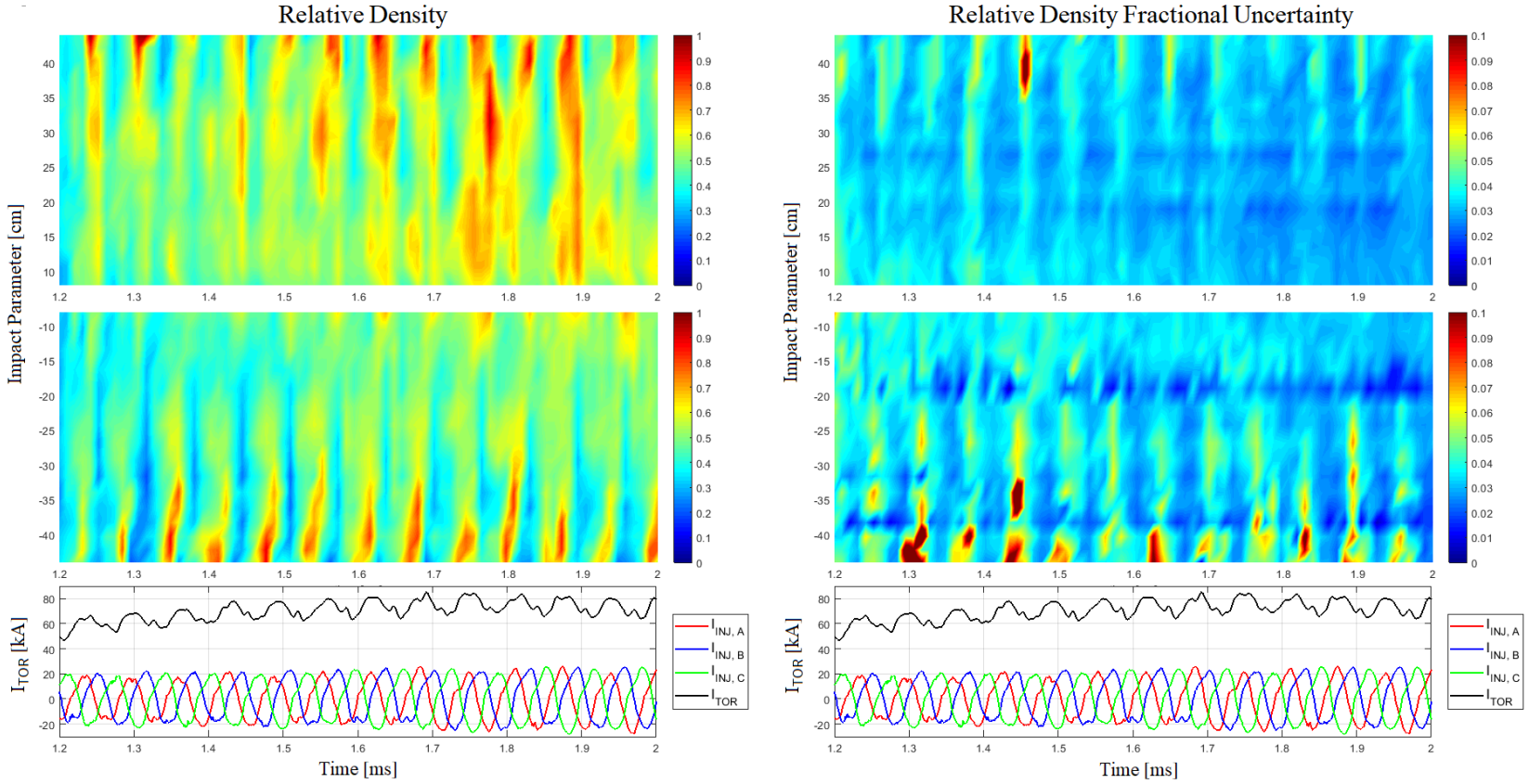

FIGURE 4.1: Deuterium plasma shot 190409014 with I_{TOR} amplification of 2.75. The normalized relative density is shown on the left and the fractional uncertainty on the right. Data points that could not be fit were box car averaged over space. Fractional uncertainty is the LMM error for the volume parameter after error propagation.

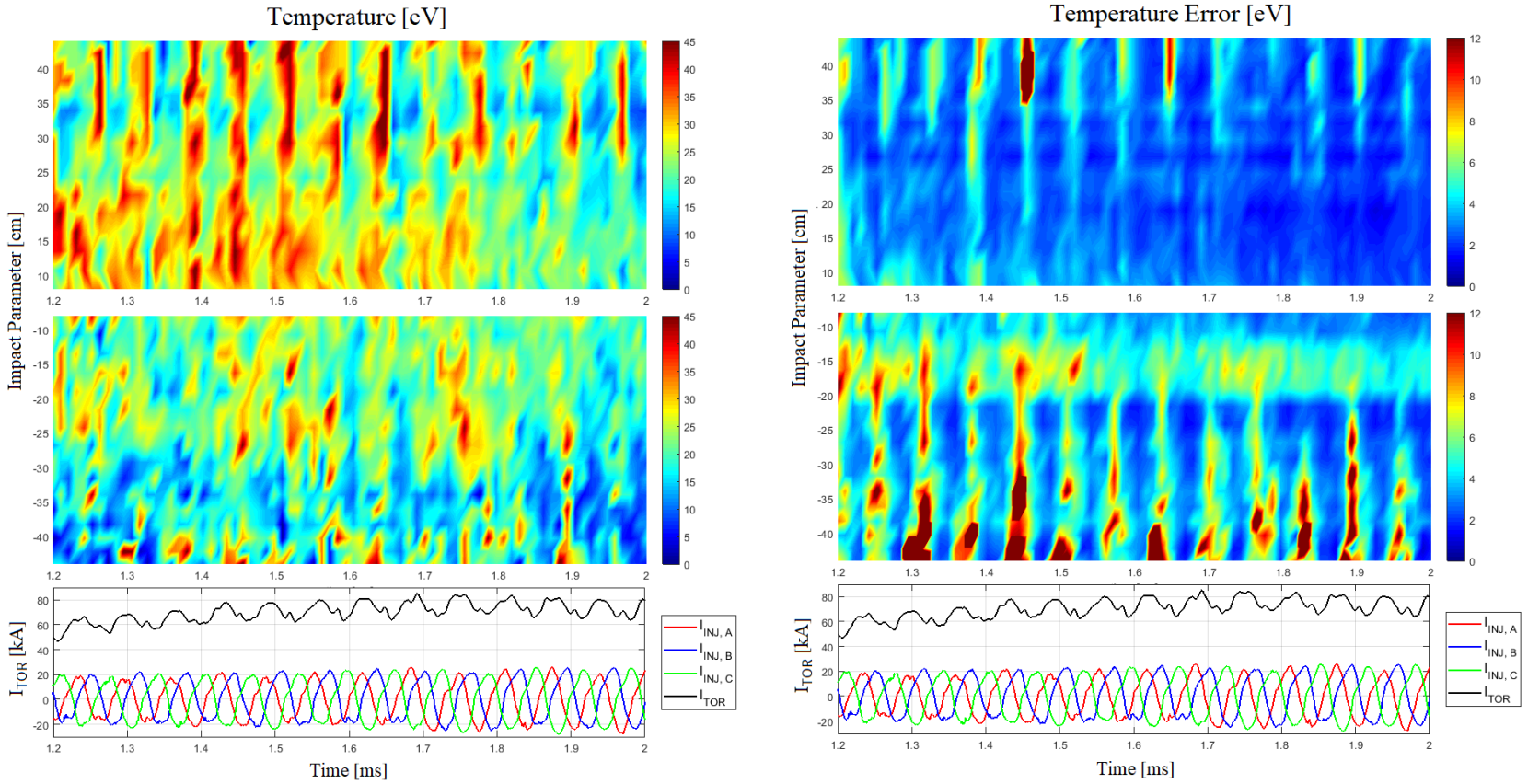

FIGURE 4.2: Deuterium plasma shot 190409014 with I_{TOR} amplification of 2.75. The temperature is shown on the left and the standard deviation on the right. Data points that could not be fit were box car averaged over space. Uncertainty is the LMM error for σ_y parameter after error propagation.

4.2 Time-Averaged Dynamics

To obtain an estimate of the midplane equilibrium profile, one can average out the injector perturbations over a time domain. This can be done for velocity by assuming the dominant basis function is periodic and based on the periodic perturbation applied by the helicity injectors. Therefore, the component of the ion motion oscillating at the injection frequency can be isolated by assuming a constant amplitude sinusoidal function. The jth channel number reconstructed velocity is fit to the functional form given by Eq. 4.2. Here A_j is the amplitude, O_j is the offset velocity, and ϕ_j is the temporal phase offset. The raw data set is fit with the LMM that uses a fast-Fourier transform (FFT) to generate the initial estimates of the fit parameters.

$$v_j(t) = A_j sin(2\pi t f_{INJ} + \phi_j) + O_j \tag{4.2}$$

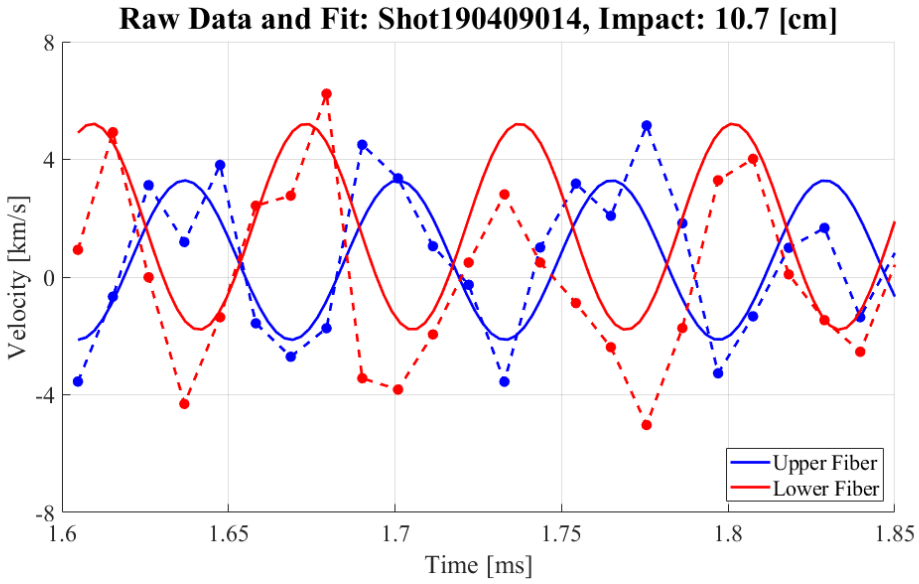

FIGURE 4.3: Raw velocity data (dashed) comparison alongside the function fit (solid) for impacts parameters ±10.7 cm for HIT-SI3 shot 190409014.

A time-averaged data comparison of CIII ions in two similar deuterium plasma shots in Fig. 4.3 compares temperature data from the upper and lower

fiber arrays for $\Delta t = 1.65 - 2.0$ ms. Δt was chosen during the plateau of I_{TOR} during which the current oscillates about a near constant value. The oscillatory perturbative effects by the injectors are assumed to be averaged out for $\Delta t \gg \frac{1}{f_{INJ}}$. The temperature values range from $12 - 28$ eV and are characterized by a spatially flat profile for low impact parameters. The overlap for the upper and lower fiber arrays between impacts parameters $8 - 25$ cm and $33 - 44$ cm indicates an axi-symmetric mean temperature distribution. Some of the lowest temperatures are the chords closest to the wall and tangent to the magnetic axis near major radius $R = 33$ cm. This may indicate that hotter ions are confined off the inner wall.

The maximum displacement for channel j (D_j) over an injection cycle is found by analytically integrating Eq. 4.2 and taking the magnitude to obtain,

$$D_j = \frac{A_j}{2\pi f_{INJ}}. \tag{4.3}$$

Axi-symmetric flow is assumed such that the channels with equal impact parameter magnitude but of opposite sign will measure opposing ion flow on average. The maximum displacement ranges from $2 - 10$ cm with all fiber arrays indicating the largest displacement occurs at impact parameter 40 ± 3 cm.

Net ion flow is calculated as half the difference between the fitted offsets.

$$F_j = \frac{(O_j - O_{-j})}{2} \tag{4.4}$$

The toroidal flow is typically zero for impacts before 20 cm. Further outward it can be seen that the net flow approaches a non-zero value with the largest value being the largest impact parameter. This corresponds to the same region of largest maximum displacement. Each fiber fitted normal distribution has an associated relative centriod shift Δy as compared to the calibration centriod y_0. $\Delta y > 0$ was set to correspond to $\Delta\lambda > 0$ and implies that the

chordal average ion flow is red shifted, traveling directly away the fiber line of sight. Therefore, negative toroidal flow is rotating counter-clockwise when viewing Fig. 2.4, the opposite direction to the toroidal electron current.

The temporal phase ϕ_j relates the average ion motion to the injector current. The injector current for the three injectors (A, B, and C) are fit with the functional form Eq. 4.2 to determine their phase. Both the injector phases and ϕ_j reference time point $t_0 = 1.65$ ms to avoid phase jumps. Phase correlations between the injectors and ϕ_j provide evidence for coherent bulk structures inside the plasma. For instance, flat regions in the temporal phase of displacement (Fig. 4.4 top) indicate that the plasma is responding to the injector perturbation instantly in that region. All fiber arrays have flat regions at a 2π multiple of an injector phase. The lower fiber of shot 190409014 shows jumps between injectors A and C. While the upper fiber of both shots indicates a steady drift from injector A to injector B with increase impact parameter.

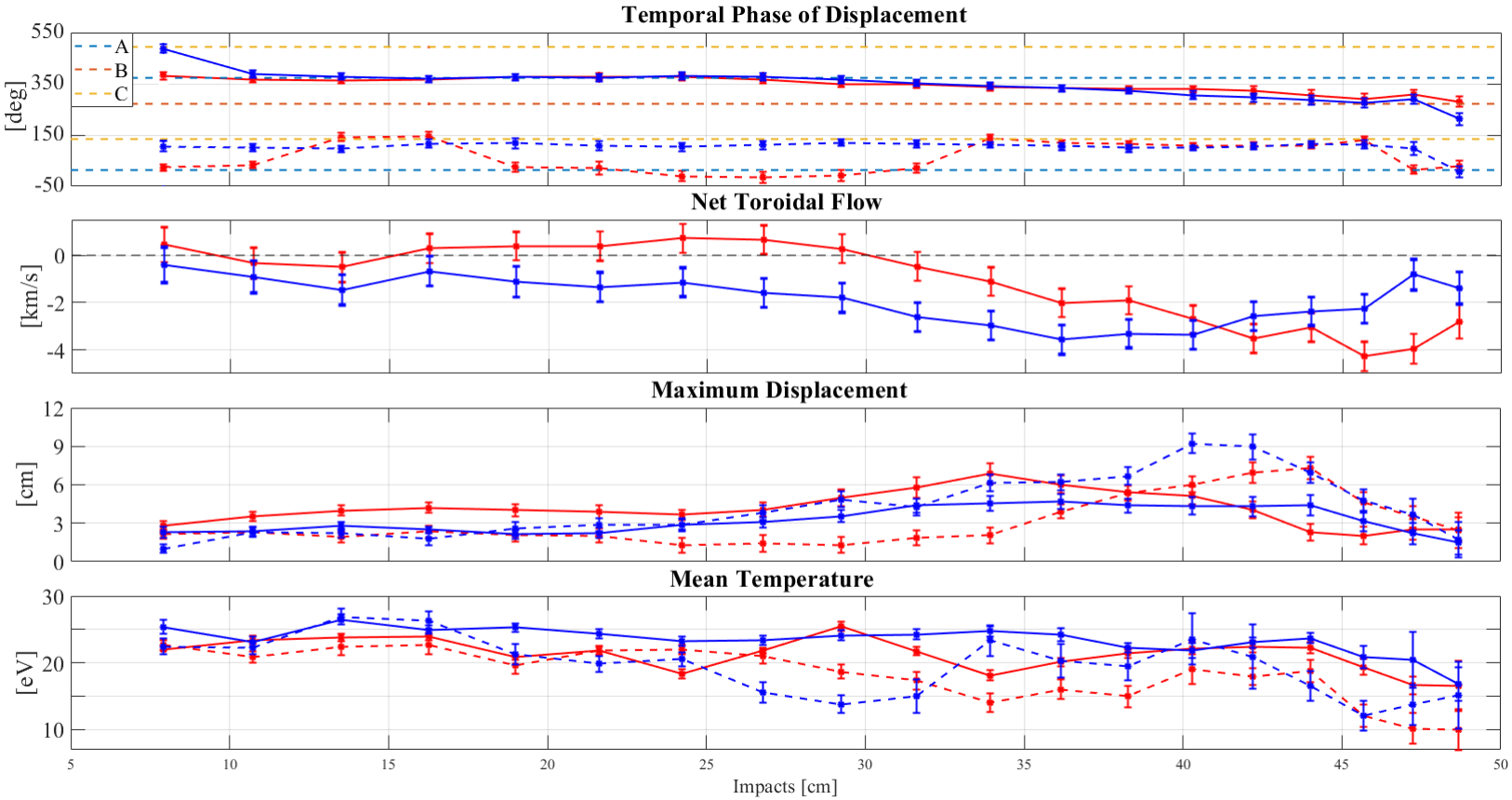

FIGURE 4.4: Comparison of CIII ion dynamics in two similar deutirium plasma shots. Shot 190409014 (red) with $I_{TOR} =$ 76.3 kA and current amplification of 2.75. Shot 190423018 (blue) with $I_{TOR} =$ 72.7 kA and current amplification of 2.85. Data is time-averaged for $\Delta t = 1.65 - 2.0$ ms. Upper fiber array data (solid) is plotted alongside the lower fiber array (dashed) for a given impact parameter. The three injector phases are also shown as horizontal, dashed lines (top).

4.3 Error Analysis of Time-Averaged Dynamics

The error presented for the displacement ($\sigma_{D_{j,k}}$), ion flow (σ_{F_j}), and temperature (σ_{T_j}) models are found by propagating the error from the Levenberg-Marquartdt algorithm output and the RMS error corresponding to the sinusoidal regression to yield:

$$\sigma_{T_{j,k}} = \sqrt{\frac{1}{N}\left(\frac{\Sigma_i^N \sigma_{T_{ij}}^2}{N^2} + std(T(t))^2\right)},$$

$$\sigma_{F_j} = \sqrt{\frac{1}{2T}\left(\Sigma_k^2 \frac{\Sigma_i^N \sigma_{v,i,j,k}^2}{N^2} + \sigma_{RMS,j,k}^2\right)}, \tag{4.5}$$

$$\sigma_{D_{j,k}} = \sqrt{\frac{1}{N(2\pi f_{INJ})^2}\left(\frac{\Sigma_i^N \sigma_{v,i,j,k}^2}{N^2} + \sigma_{RMS,j}^2\right)}.$$

Here i is the number of time points associated with the impact parameters of fiber j from fiber array k of 2. The number of time points is N and σ_{RMS} is the RMS error associated with Eq. 4.2. The last two quantities are $\sigma_{v,i,j,k}$ and $\sigma_{T_{ij}}$ which are the LMM velocity and temperature error respectively each corresponding to i, j, or k shown in the subscripts. The error shown for the temporal phase of displacement come directly from the sinusoidal RMS error.

4.4 Abel Inversion of Chord-Averaged Measurements

In plasma experiments it is often the case that the physical quantity of interest cannot be measured directly as a function of radius. Physical probes have been known to perturb the plasma that it's trying to measure and the extreme environment inside hotter plasmas can make it inaccessible to physical probes past surface depth. Analyzing light along a path length through

the plasma is a common non-pertubative diagnostic technique that can yield valuable information. These techniques are limited to chord-averaged measurements as there is no way of distinguishing local phenomena along the path. Although, given cylindrical symmetry, chord-averaged data can be inverted to give information about a spatial profile without introducing significant error. HIT-SI3 is radially symmetric about its geometric axis. This makes it possible for chord-averaged measurements to be unfolded into a major radial profile using Abel inversion techniques. The numerical method employed for this paper was created by G. Pretzler[18] and is summarized here.

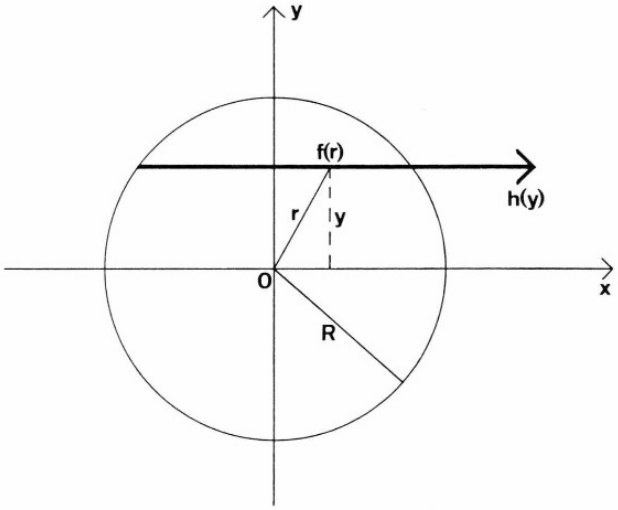

FIGURE 4.5: Plasma column of radius R with cylindrical symmetry depicting a chord-averaged measurement $h(y)$ a distance y from the origin along a path in the x-direction. The measurement can then be inverted to give a measurement $f(r)$ at the corresponding radius r.[18]

Using the geometry in Fig. 4.5, any scalar plasma parameter measured on a chord of length L will have an integrated value given by,

$$h(y) = \int_{-L/2}^{L/2} f(r)dx \tag{4.6}$$

which can be converted using a change in variables.

$$h(y) = 2\int_y^R \frac{f(r)r}{\sqrt{r^2 - y^2}}dr \tag{4.7}$$

Eq. 4.7 is one of Abel's integral equations. The integral is often impossible or at least impractical to solve in most experiments without cylindrical symmetry. Given this symmetry the problem becomes one dimensional, and can be analytically solved. Given $r = 0$ for $r > a$, this equation can be inverted to produce:

$$f(r) = -\frac{1}{\pi}\int_r^R \frac{dh(y)}{dy}\frac{f(r)r}{\sqrt{y^2 - r^2}}dy \tag{4.8}$$

Numerical solutions of Eq. 4.8 usually suffer from random experimental noise amplification from the evaluation of the derivative. This can be alleviated by fitting a smooth function before inversion.

This numerical Abel inversion method is derivative free and doesn't require smoothing or any other pre-treating of the measured data $h(y)$. The unknown radial distribution $f(r)$ is expanded in a series similar to a Fourier-series:

$$f(r) = \Sigma_{N_l}^{N_u} A_n f_n(r) \tag{4.9}$$

where A_n are unknown amplitudes and $f_n(r)$ is a set of cosine-functions, e.g.

$$f_0(r) = 1, \qquad f_n(r) = 1 - (-1)^n cos\left(\frac{n\pi r}{R}\right). \tag{4.10}$$

Mirroring the form in Eq. 4.7, the Abel-transform $H(y)$ also has the form

$$H(y) = 2\Sigma_{n=N_l}^{N_u} A_n \int_y^R \frac{f_n(r)r}{\sqrt{r^2 - y^2}}dr \tag{4.11}$$

Each integral,

$$h_n(y) = 2\int_y^R \frac{f_n(r)r}{\sqrt{r^2 - y^2}}dr \tag{4.12}$$

is evaluated in advance in the numerical routine. Eq. 4.11 is fit with a least squares regression to the real data $h(y)$ at each N measured points y_k:

$$f(r) = \Sigma_{k=1}^{N} \left(H(y_k - h(y_k)\right)^2 \rightarrow \min, \tag{4.13}$$

producing a system of equations:

$$\Sigma_{n=N_l}^{N_u} A_n \Sigma_{k=1}^{N} \left(h_n(y_k)h_m(y_k)\right) = \Sigma_{k=1}^{N} h(y_k)h_m(y_k), \qquad \forall N_l \leq N < N_u \tag{4.14}$$

allowing the unknown coefficients A_n to be determined and inserted into Eq. 4.9. For the analysis presented in further sections the system is solved by a MATLAB non-linear least squares algorithm. The amount of expansion terms N_u are chosen to be less than half the amount of data points. Less expansion terms give a smoothed profile that reduces error from noise, while keeping more terms makes the inversion more responsive to higher order characteristics; a point that will be expanded upon in a further section.

4.4.1 Radial Relative Density

A calculation of the midplane toroidal equilibrium profile as a function of major radius is calculated using the expansion based Abel inversion technique described in Section 4.4 for relative density, velocity, and temperature. $N = 25$ chord-averaged measurements are used from near the geometric axis located at major radius $R = 0$ through the projection of the magnetic axis on the midplane at $R \approx 33$ cm to about $R \approx 49$ after which there is no appreciable signal. The wall is set to zero at the boundary $R_{wall} = 55.5$ cm as the path integral is zero. The inversion of chord impact parameters to a function of major radius that is symmetric about the magnetic axis. The series in Eq.

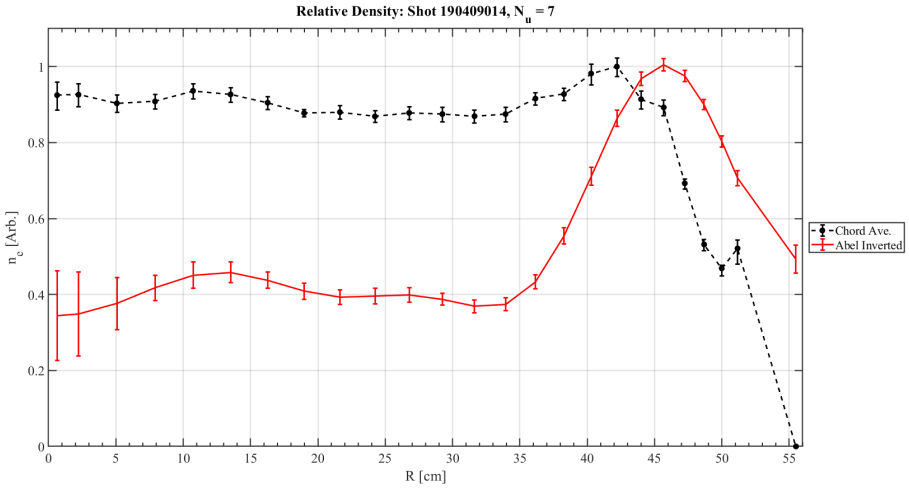

FIGURE 4.6: Time-averaged relative density chord measurements (black) are compared against the Abel inverted major radial profile (red) for HIT-SI3 shot 190409014 from the geometric axis ($R = 0$ cm) to the wall ($R = 56$ cm). The time window under consideration is $\Delta t = 1.637 - 1.703$ ms.

4.9 is truncated at $N_u = 7$ to smooth the effect of random noise in the data. Therefore, the profile neglects large gradients in the data and essentially acts as a low pass filter.

To calculate the relative electron density profile, the intensity measurements along each chord are time-averaged over a complete injector cycle $\Delta t = 1.637 - 1.703$ ms and scaled with Eq. 4.1. The upper and lower fiber are averaged together. Δt is chosen to reduce magnetic axis radial drift which can be up to 10 cm. The red radial profile shown in Fig. 4.6 has a near uniform density up to about the magnetic axis where it then increases to the maximum value at $R = 45.5$ cm before decreasing to finite values at the wall. The largest fractional uncertainty is near the geometric axis and is ± 0.2 while the remaining values have an uncertainty of about ± 0.05.

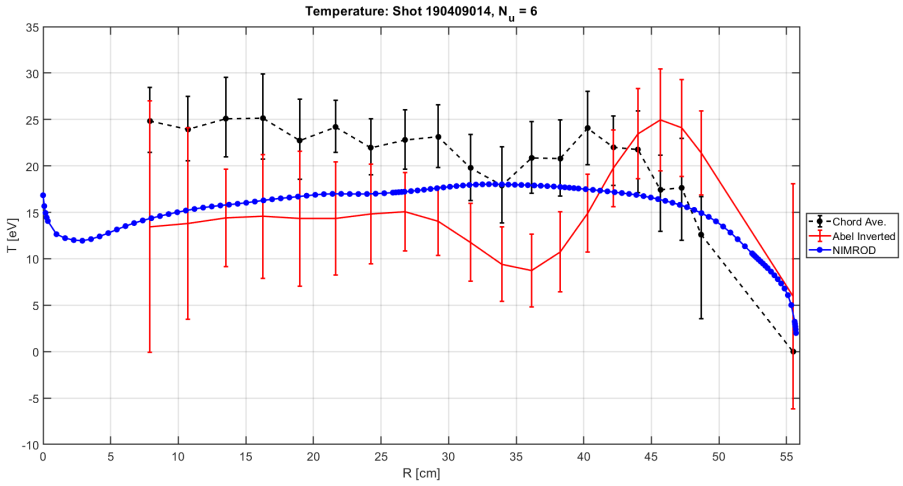

FIGURE 4.7: Time-averaged temperature chord measurements (black) are compared against the Abel inverted, $N_u = 6$, major radial profile (red) for HIT-SI3 shot 190409014 from the geometric axis ($R = 0$ cm) to the wall ($R = 56$ cm). Upper and lower fiber bundles have been averaged. A simulated radial profile calculated using NIMROD (blue) is also shown for HIT-SI3 shot 160609009. The time window under consideration is $\Delta t = 1.2 - 2.0$ ms for all.

4.4.2 Radial Temperature

Chord-averaged temperature data are Abel inverted into a major radial profile. Also, this radial inversion is compared to a NIMROD simulation. NIMROD is a spatially 3D, extended MHD code modeled with a discretized box-tie flux conserver matching the dimensions of HIT-SI3. The simulation uses shot 160609009 ($f_{INJ} = 14.5$ kHz) as the input waveforms for the injectors and are imposed through boundary conditions of the confinement volume on a set of four time-evolved Hall-MHD equations; the continuity equation, momentum equation, Faraday's law, and the energy equation. Other plasma parameters that match those of the experiment include injector flux, toroidal current, density, resistivity, viscosity, and Alfvn time. The electron mass is enhanced to $1/36^{th}$ of the ion mass for numerical stability and speed. To obtain a radial temperature profile, the simulated data is toroidally averaged on

the midplane. The simulation shown in Fig. 4.7 and the following paragraph were both implemented by Kyle Morgan.

The upper and lower fiber array chord temperatures are time-averaged over $\Delta t = 1.2 - 2.0$ ms and then two arrays themselves are averaged and plotted in Fig. 4.7 along with the Abel inverted profile, and the simulated NIMROD profile. The Abel inverted temperature has large uncertainty. The only significant features that can be discerned are a small dip in temperature near the magnetic axis and a possible peak in temperature at $R = 45.5$ cm. Again the error is greatest at the geometric axis an the wall. The NIMROD profile shows similar temperatures but is flatter. Taking both radial profiles together show a decrease in temperature towards the wall but the significance of either profile on its own is questionable.

4.4.3 Radial Velocity

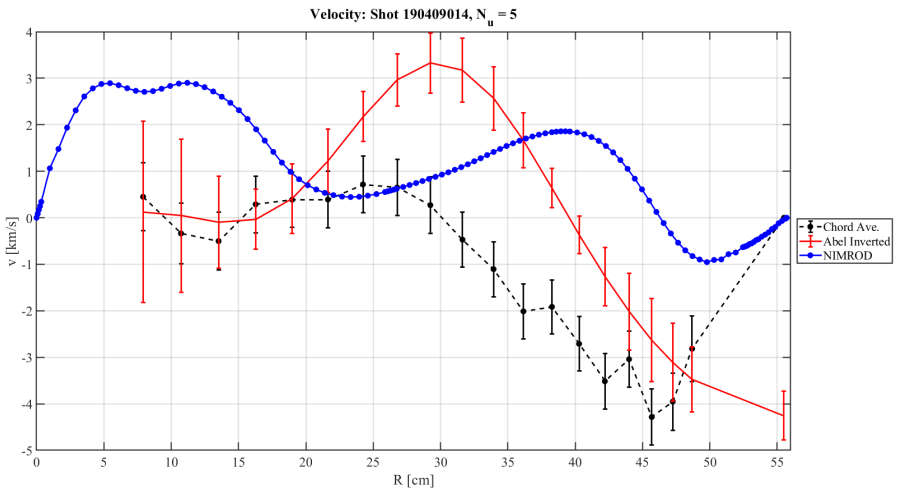

FIGURE 4.8: Time-averaged velocity chord measurements (black) are compared against the Abel-inverted, $N_u = 6$, major radial profile (red) for HIT-SI3 shot 190409014 from the geometric axis ($R = 0$ cm) to the wall ($R = 56$ cm). A simulated radial profile calculated using NIMROD (blue) is also shown for HIT-SI3 shot 160609009. The time window under consideration is $\Delta t = 1.2 - 2.0$ ms for all.

The chord-averaged ion velocity measurements are time averaged over $\Delta t = 1.2 - 2.0$ ms and are displayed (black) in Fig. 4.8. These measurements show a very small but significant positive net flow form $R = 20 - 30$ cm. While further out a large negative flow is dominant. The Abel-inverted profile is in red and discerns no net flow from the geometric axis to about $R = 20$ cm but implies a larger positive flow that peaks near the magnetic axis. The ion flow then reverses direction at $R = 40$ cm and persists to the wall. This implies that there may be ion flow in the spheromak that goes in the same direction as the toroidal current. While further out, possibly in the injector flux region, the ion flow goes against the toroidal current. While the characteristic shapes of the Abel and NIMROD profiles are noticeably different, the NIMROD simulation also shows this trend. A positive current (before $R = 46$ cm) before changing direction further radially outward.

4.5 Abel Inversion Error

In order to understand the error imposed by the inverse Abel transform, a synthetic radial function $F(R)$ is used in a fitting domain from the magnetic axis to the wall for the same number of measurements ($N = 10$) as the preceeding radial profiles has in this domain. $F(R)$ is a fourth order polynomial of the form $F(R) = aR^4 + bR^3 + cR^2 + d$ where coefficients a, b, and c are chosen such that $F(R)$ is normalized and goes to zero at the boundary $R_{wall} = 55.5$ cm. An Abel transform given by Eq. 4.12 is applied to FR to yield the synthetic chord-averaged measurement profile $f(y)$.

To imitate actual chordal measurements, $f(y)$ is superimposed with a layer of noise. The noise for each data point (except at R_{wall}) is randomly selected to acquire a value of $\pm(N/S)_{max}$. Here, $(N/S)_{max}$ is the bounds of the noise to maximam signal ratio ($S = f(y)_{max}$). E.g. if $(N/S)_{max} = 10\%$ and $f(y_{max}) = 1$, then a pseudo-random number generator prescribes a noise

value between ± 0.1 to each data point. The noisy chord profile is then Abel inverted with the same process outlined in Section 4.4 to give the reconstructed radial profile $f(R)$ for a comparison of the error $\Delta f = f(R) - F(R)$.

First, the truncation term N_u for the Abel inversion series solution needs to be determined. First, the upper truncation term must be less than the number of data points for the method to well defined ($N_u < N$). Next, the metric used to estimate the overall best fit between the reconstructed distribution and the actual distribution is the residual sum of squares (RSS) and is shown in Eq. 4.15.

$$RSS = \Sigma_1^{N_u} \Delta f^2 \tag{4.15}$$

For $\pm(N/S)_{max} < 10\%$ it was found that $N_u > 1$ all give approximately the same RSS. In the case of $\pm(N/S)_{max} > 10\%$, $N_u = 2$ was found to be a minimum in the majority of trials varying $10\% < (N/S)_{max} < 30\%$ with the exception of $N_u = 3$. A representative trial is shown in Fig. 4.9 where $(N/S)_{max} = 20\%$.

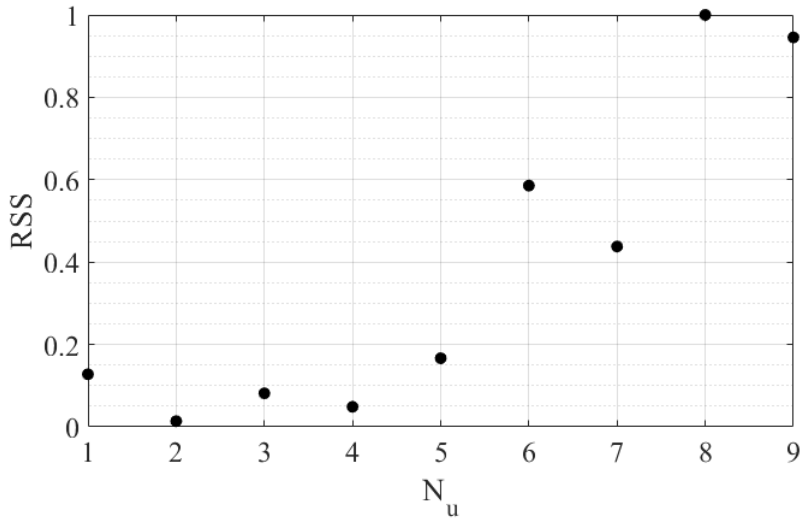

FIGURE 4.9: The normalized residual sum of squares RSS of the error function Δf for increasing series truncation term N_u. The number of data points is $N = 10$ and $(N/S)_{max} = 20\%$

When the noise in the data is about 20% the most accurate inversion tends to have a N_u that minimizes the RSS before more terms cause the method to diverge from the solution. This trend persists for differing number of measurement points N. The RSS tends to reach a minimum when $N_u \approx 1/3N$. This provides reasonable cause to select $N_u = 5 - 7$ for the various Abel inversions used in the previous sections for T_i, n_e, and F_i. Although, it is still unknown whether a different selection of N_u would provide a better match to the actual radial distribution.

All data shown in Fig. 4.10 uses $N_u = 2$ and the two profiles use $(N/S)_{max} = 20\%$. As $(N/S)_{max}$ increases, the error about the axis of symmetry becomes more pronounced as is apparent in the graphs on the right. $(N/S)_{max} = 0\%$ results in at most 2.5% error but $(N/S)_{max} = 30\%$ results in at most $\approx 50\%$ error. The error at R_{wall} also shows sensitivity to measurement error. Whether the reconstructed distribution overshoots or undershoots the areas of maximum error were dependent on the values of noise.

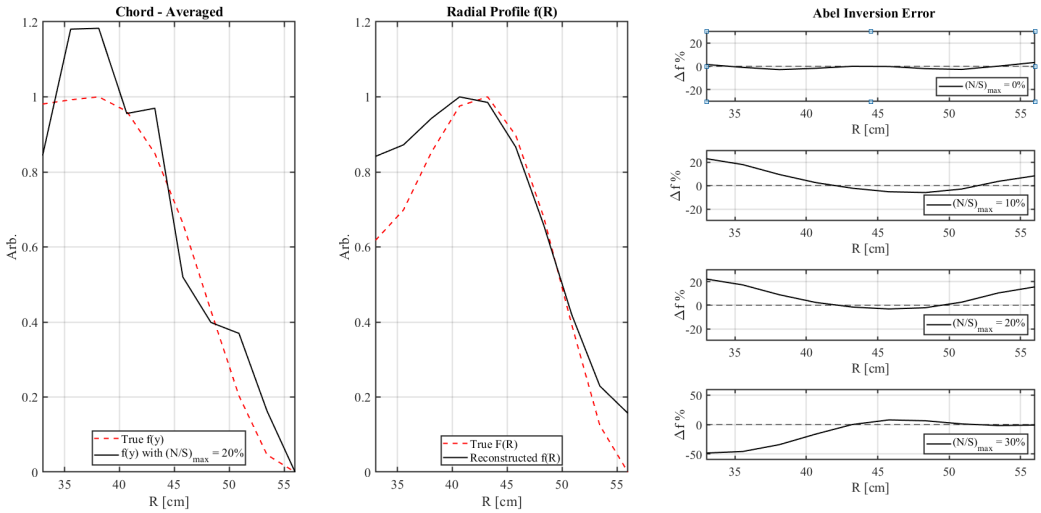

FIGURE 4.10: Chord-averaged measurments are shown on the left figure, radial profiles in the middle figure, and the radial profile error for different random noise levels on the right. The synthetic profiles are shown as dashed red and the noisey chord measurments and reconstructed radial profile are in solid black. The radial error is reported as $\Delta f = f(R) - F(R)$.

To quantify the error for real data a Monte Carlo method was developed. The *jth* chord-averaged quantity $f(y_j)$ have their respective uncertainties summed in quadrature to obtain the time-averaged σ_j. Next, a random value generated from a normal distribution described by $N(f(y_j), \sigma_j)$ replaces $f(y_j)$ for each point $1 \leq j \leq N$. The new altered function $\hat{f}(y_j)$ is then inverse transformed to give $\hat{f}(R_j)$. This process is iterated $1,000$ times to obtain a mean and standard deviation at each spatial point. The means are assigned to the final reconstructed fit $f(R_j)$ with a standard deviation characterized by the spread of iterated inverse transforms.

As expected, the largest error obtained in the data presented in Section 4.4 is about the magnetic axis and R_{wall}. This method of quantifying error allows for a N_u to be selected and that shows the least variation over many iterations. Inversion profiles that have the least variation are then assumed to be the closest to the actual profile and ultimately determined the selection of N_u for the Abel inverted quantities.

Chapter 5

Conclusions

5.1 Summary

Experimental results obtained from IDS on HIT-SI3 show that there is coherent bulk plasma motion locked to the injector's perturbations. Coherent motion indicates stability. Equilibrium time-averaged measurements show a phase-locked region between impacts parameters $35 - 45$ cm where maximum toroidal displacement and flow can be discerned along the chord. This makes sense if the ion velocity mostly lie in the toroidal direction as chords with impact parameters less than $\approx R_{wall}/2 = 28$ will be increasingly perpendicular to the flow until the chord goes through the geometric axis, and cannot detect pure toroidal flow. The peak of the displacement occurs at about 40 cm is consistent where the outboard seperatrix is expected to form.[15]

The Abel inversion profiles both show that there is a region at about $R = 45.5$ cm where the ion temperature and electron density is maximum. The profiles suggest that the reason why the time-averaged chord measurements are flat, especially with low impact parameter, is because the chord is integrating through a temperature peak before it enters a temperature valley near the magnetic axis. Temperature confinement near the wall is uncertain in the Abel inversion but the NIMROD simulation indicates that the temperature is indeed near 5 eV. While a temperature gradient near the wall is possible, a more accurate measurement needs to be made.

The electron density is assumed to be proportional to the CIII ion density because CIII ionization rate is assumed to be proportional to the electron density distribution. This would not be true if CIII density significantly varies throughout the confinement volume in a way that the electrons do not. For example, if a localized dense shell of electrons exists in an under dense shell of CIII then this assumption might not hold. As CIII would not have time to decay before another electron collision event and thus reduce the intensity. The intensity would instead scale as $I_{ij}\ n_e n_{ion}$. A similar effect would happen if electrons were to cold to ionize CIII. n_{ion} would then be considered a strong function of electron temperature.[10] This is a primary worry when making these comparisons as estimates for impurity density and the rate coefficient of excitation are currently unavailable in HIT-SI3.

At present, a tomography diagnostic is being built for HIT-SI3 and uses a high speed camera with 1 μs time resolution and two fiber bundles each with a 128x128 array of fiber optic cables. Each fiber array was places several inches apart on toroidal midplane ports with frequency pass band filters to select for CIII $=$ 465.18 nm and CII $=$ 658.67 nm spectral lines. To help qualitatively understand the measured C_{III} dynamics, Fig. 5.1 shows two time frames for comparison. CII has a fairly more uniform distribution near the wall, indicating a cooler temperature. C_{III} has its highest intensity further radially off the wall with a dimmer center where where you would expect the magnetic axis to be. This provides evidence that either high density electrons are inducing excitation in CIII at $R = 45.5$ cm but not near the cooler wall as indicates by the higher CII concentrations. Hence, the coronal equilibrium approximation may fail near the wall. The electron density is not expected to decrease in the region from $R = 45.5$ to the wall since a current is driven at the edge by the injectors.

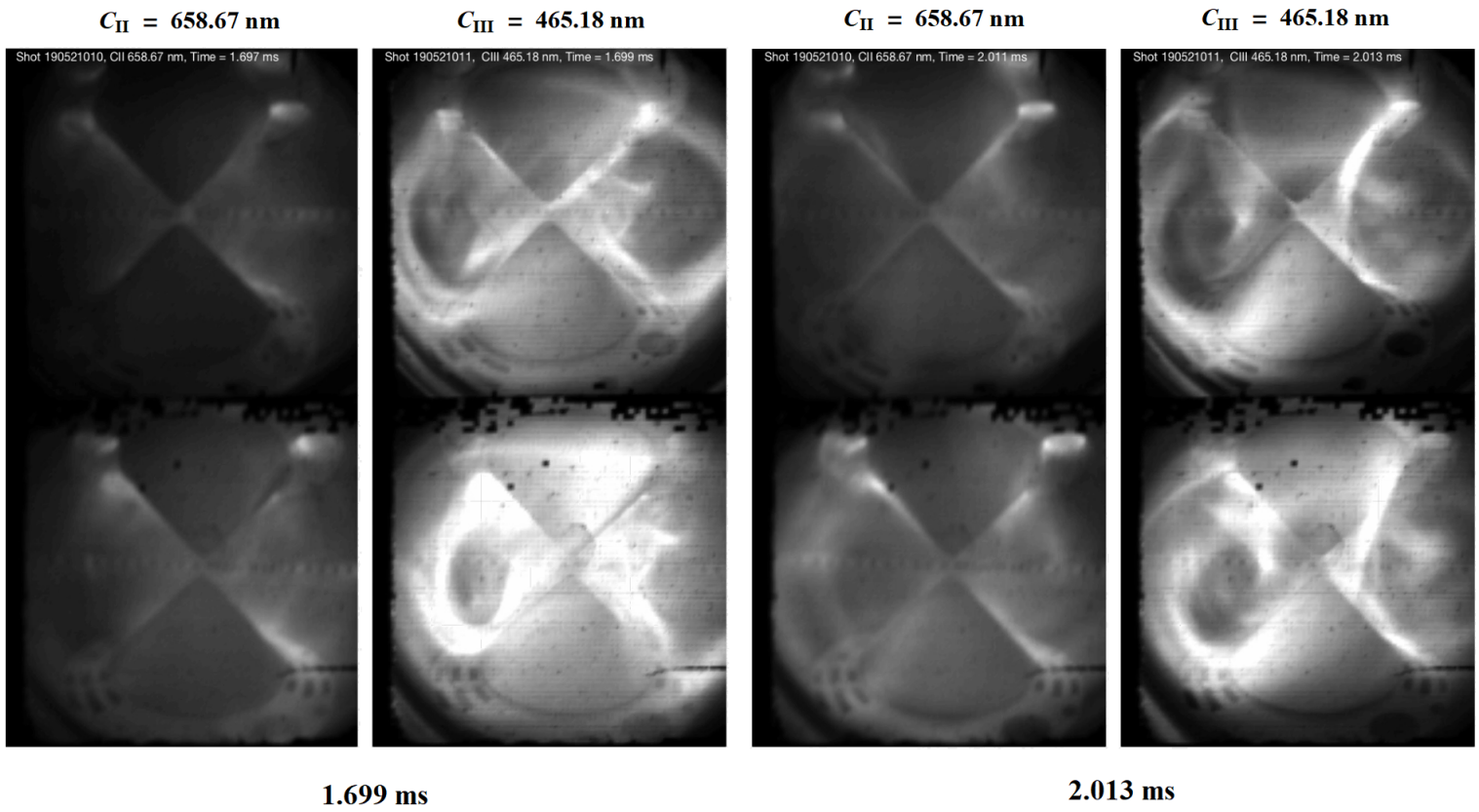

FIGURE 5.1: CIII = 465.18 nm and CIII = 658.67 nm shown for time points 1.699 ms (left) and 2.013 ms (right) on the toroidal midplane with the tomography camera for He-doped deuterium shot 190521010. Provided by Aaron Hossack.

Another factor that needs to be considered is that the ion temperature suffers from some amount of systemic error. It's possible that the ion temperature broadening is partially due to differential ion flow both toward and away on a chord within the IDS camera exposure time (10 μs) as simulations show a large amount of non axi-symmetric flow. One possibility is the ions are oscillated along a chord at the Alfvn speed which is several orders of magnitude faster than the exposure time. The effect would be seen as an artificial increase in the temperature in areas impacted by this type of motion.

5.2 Future Work

The IDS diagnostic currently has no absolute velocity calibration and velocity is estimated assuming equilibrium axi-symmetric flow. This is due to the fact that there is no known spectral line that can appear on the CCD without having to redial the spectrometer grating to the operating wavelength. The dial is not sensitive enough to read the wavelengths to the precision necessary, a line must be found when the spectrometer is already dialed to the region of interest. The CCD can detect a 3 nm window centered about 465 nm. If a known spectral line produces by a gas with zero ion velocity (like a pen lamp or laser) could be found within this range, a reference point for each chord could be calibrated and time dependent, chord averaged velocities could be measured.

One promising spectral emission candidate is the 465.8 nm line emitted from an Ar-ion laser. Recently, a Coherent Innova 90 Ar-ion laser was obtained and renovated for HIT-SI3. The water cooling system was updated and the power supply connector rebuilt. Testing will begin after the necessary optics are in place to safely operate the laser. If found to be successful, the laser could drastically improve both the spatial and temporal resolution of IDS.

There is still a large parameter space to be measured by IDS. This includes adjustments to f_{INJ}, I_{TOR}, camera exposure time, and current gain. There are many variations which could increase the intensity enough to resolve other spectral lines without hurting resolution. If another CIII line is resolved, the ratio of intensities could eliminate the dependence on impurity ion density when calculating electron density. Furthermore, there are still optimizations to be made on the Abel inversion technique. The inversion profiles can also be compared to newer MHD simulations such as PSI-Tet which more accurately model the full geometry of the helicty injectors.

Bibliography

[1] Juan Carlos Santamarina Cesar Pasten. “Energy and quality of life”. In: *Energy Policy* (2012).

[2] Internationl Energy Agency. “World Energy Outlook”. In: *IEA Publications* (2016).

[3] Corinne Le Quéré et al. “Global Carbon Project”. In: *Earth System Science Data* 10.1-54 (Dec. 2018).

[4] Scott Waldman. “Global CO2 nears troubling benchmark”. E&E News.

[5] Jeffrey Freidberg. *Plasma Physics and Fusion Energy*. Cambridge University Press, 2007. ISBN: 978-0-521-73317-5.

[6] D.A. Sutherland et al. “The dynomak: An advanced spheromak reactor concept with imposed-dynamo current drive and next-generation nuclear power technologies”. In: *Fusion Eng. Des.* 89.4 (Apr. 2014), pp. 412–425.

[7] T.R. Jarboe. “Steady inductive helicity injection and its application to a high-beta spheromak”. In: *Fusion Science and Technology* 36(1) (1999), :85–91.

[8] T.R. Jarboe et al. “Imposed-dynamo current drive”. In: *Nucl. Fusion* 52.083017 (2012).

[9] Wesson J. “Tokamaks”. In: *Tokamaks* (1987).

[10] I. H. Hutchinson. *Principles of Plasma Diagnostics Second edition*. Ed. by Cambridge University Press. 2002.

[11] George Schmidt. *Physics of High Temperature Plasmas*. New York : Academic Press, 1979.

[12] Aaron Hossack et al. "Improvements to the ion Doppler spectrometer diagnostic on the HIT-SI experiments". In: *AIP Review of Scientific Instruments* (2018).

[13] N. Konjevıc et al. "Experimental Stark widths and shifts for spectral lines of neutral and ionized atoms: A critical review of selected data for the period 1989 through 2000". In: *J. Phys. Chem. Ref. Data* 31(3).819 (2002).

[14] T. Odstrcil. "Study of visible plasma radiation by high resolution spectroscopy at additional plasma heating by neutral beams injection on the COMPASS tokamak". PhD thesis. Czech Technical University in Prague, 2012.

[15] A.C. Hossack. "A Study of Ion Dynamics in HIT-SI Using Ion-Doppler Spectroscopy". PhD thesis. University of Washington, 2015.

[16] Henri Gavin. *The Levenberg-Marquardt method for nonlinear least squares curve-fitting problems*. Department of Civil and Environmental Engineering Duke University. 2011.

[17] Gaetz et al. "Line radiation from a hot, optically thin plasma - Collision strengths and emissivities". In: *Astrophysical Journal Supplement Series* (1983).

[18] G. Pretzler. "A New Method for Numerical Abel-Inversion". In: *Zeitschrift für Naturforschung A* (1991).